



4-2007

Development of Scanning Electrochemical Microscopy for Studying Electron Transport in Lipid Monolayers and Gold Nanoparticle Films

Violeta Stoycheva

Follow this and additional works at: https://scholarworks.wmich.edu/masters_theses



Recommended Citation

Stoycheva, Violeta, "Development of Scanning Electrochemical Microscopy for Studying Electron Transport in Lipid Monolayers and Gold Nanoparticle Films" (2007). *Master's Theses*. 4410.
https://scholarworks.wmich.edu/masters_theses/4410

This Masters Thesis-Open Access is brought to you for free and open access by the Graduate College at ScholarWorks at WMU. It has been accepted for inclusion in Master's Theses by an authorized administrator of ScholarWorks at WMU. For more information, please contact wmu-scholarworks@wmich.edu.



DEVELOPMENT OF SCANNING ELECTROCHEMICAL MICROSCOPY FOR
STUDYING ELECTRON TRANSPORT IN LIPID MONOLAYERS AND
GOLD NANOPARTICLE FILMS

by

Violeta Stoycheva

A Thesis
Submitted to the
Faculty of the Graduate College
In partial fulfillment of the
requirements for the
Degree of Master of Science
Department of Chemistry

Western Michigan University
Kalamazoo, Michigan
April 2007

Copyright by
Violeta Stoycheva
2007

ACKNOWLEDGEMENTS

First and foremost, I would like to greatly acknowledge my supervisor Professor Dongil Lee for his continuous encouragement and guidance in this work.

I am very grateful to my committee members, Dr. Subra Muralidharan and Dr. Brian Tripp for all the Keck meetings, discussions, and constructive suggestions during my research.

I am also thankful to Dr. Narayanan Srividya for helping me with the lipid study. I would like to thank all my group members Jun, Mariana, Hye-Young, and Princess for an enjoyable environment including great discussions.

I am also greatly indebted to my husband for always being around and looking after me. Finally, I would like to thank my grandma and my family for all the love, patience, and support they showed over the years.

Violeta Stoycheva

DEVELOPMENT OF SCANNING ELECTROCHEMICAL MICROSCOPY FOR STUDYING ELECTRON TRANSPORT IN LIPID MONOLAYERS AND GOLD NANOPARTICLE FILMS

Violeta Stoycheva, M.S.

Western Michigan University, 2007

The focus of this thesis is the scanning electrochemical microscopy (SECM) investigation of the electron transport in lipid monolayers and in films of gold nanoparticles. The quality and stability of lipid monolayers were characterized by various analytical techniques such as fluorescence microscopy and spectroscopy, contact angle, and electrochemistry using a monolayer modified electrode. In the SECM measurement, the monolayer electron transport was not detected. The microscopic monolayer quality turned out to be not suitable for studying the electron transport.

The conductivity of monolayer protected gold clusters (MPCs) with different core sizes (1-3 nm diameter) were investigated using SECM. These AuMPCs were characterized by UV-VIS, voltammetry, and transmission electron microscopy (TEM). In SECM measurements, the film conductivity has been extracted from the feedback currents. The conductivity appears to be dependent on the MPC core size, but the dependence becomes weaker with core size dispersity. The disordering effect on the film conductivity was investigated along with the core size effect.

TABLE OF CONTENTS

ACKNOWLEDGEMENTS	ii
LIST OF TABLES	v
LIST OF FIGURES	vi
CHAPTER	
I. INTRODUCTION.....	1
1.1 Scanning Electrochemical Microscope (SECM).....	1
1.2 Electron transport through thin organic films	4
1.3 Central hypothesis and structure of proposed research	7
II. EXPERIMENTAL SECTION	10
2.1 Materials.....	10
2.2 Langmuir-Blodgett trough.....	11
2.3 Fluorescence microscopy	13
2.4 UV-VIS and fluorescence spectrometers	14
2.5 Contact angle measuring instrument	14
2.6 Electrochemistry with modified ITO	15
2.7 Scanning Electrochemical Microscopy (SECM)	15
2.8 Disk microelectrode fabrication	17
2.9 AuMPCs synthesis	20
2.10 Electrochemistry of AuMPCs	23

Table of Contents - Continued

CHAPTER

2.11 Transmission electron microscope (TEM)	25
III. DEVELOPMENT OF SCANNING ELECTROCHEMICAL MICROSCOPY (SECM).....	26
3.1 Characterization of a fabricated SECM tip	27
3.2 Simulation of a SECM experiment	31
IV. SECM STUDY OF LIPID MONOLAYERS.....	39
4.1 Lipid monolayers of different chain-lengths at the air/water interface	41
4.2 Langmuir-Blodgett transfer of lipids to a solid substrate	45
4.3 Redox probe incorporated lipids for SECM measurements: DmFc-DMPC .	52
4.4 Contact angle measurements	58
4.5 ITO electrochemistry.....	60
V. SECM STUDY OF AuMPCs FILMS	64
5.1 $\text{Au}_{38}(\text{SC}_6\text{H}_{13})_{24}$ – characterization and conductivity	67
5.2 $\text{Au}_{140}(\text{SC}_6\text{H}_{13})_{53}$ – characterization and conductivity	72
5.3 Conductivity of samples A and B	75
VI. CONCLUSIONS AND FUTURE DIRECTIONS.....	80
REFERENCES	84
APPENDICES	89
A. MATLAB PROGRAM.....	89
B. PERMISSION LETTER.....	99

LIST OF TABLES

1. Collapse surface pressure, phase transition temperature, and the area occupied by one molecule for saturated lipids with chain lengths of C10, C12, C14, C16, C18, and C20. DDPC and DLPC are in fluid phase at room temperature, DMPC is in phase transition, and DPPC, DSPC, and DAPC are in gel phase. 43
2. Formal potentials and diffusion coefficients of five redox couples..... 54
3. Static contact angles of a water drop on different substrates. 59

LIST OF FIGURES

1. A selection of modes of operation of a SECM with an amperometric ultramicroelectrode tip.	2
2. Langmuir-Blodgett trough. 1-Surface tension sensor, 2-Substrate for deposition, 3-Dipper mechanism, 4-Barriers for monolayer compression and expansion.	12
3. Langmuir-Blodgett technique for monolayer transfer.	13
4. Epi-flourescence microscope Nikon Eclispe.	14
5. SECM apparatus. 1-Bipotentiostat & data acquisition, 2-Tip holder, 3-XYZ tip positioners, 4-Electrochemical cell, 5-Substrate electrode	16
6. A: Clean borosilicate capillary tube and B: torch sealed capillary tube.	18
7. The capillary is aligned with a resistor coil.	18
8. Sealed 25 μm diameter Pt wire in a capillary tube resulted from coil heating.	19
9. A: Injection of conductive silver epoxy around the Pt wire and B: Introduced Cu wire in the capillary tube for electrical contact with the Pt wire.	19
10. Polished SECM tip. A: Example of a mispolished tip and B: Image of a successfully polished tip.	20
11. UV-VIS spectra of AuMPCs in dichloromethane. The spectra are normalized to unity absorbance at 300 nm.	22
12. TEM images of (A) $\text{Au}_{38}(\text{SC}_6\text{H}_{13})_{24}$; (B) $\text{Au}_{140}(\text{SC}_6\text{H}_{13})_{53}$; (C) AuMPCs (1:3); (D) AuMPCs (1:1). Insets show the histograms of the core diameter, where the standard deviations from the mean is displayed.	23
13. Cyclic voltammogram of 1mM FcMeOH in 0.1 M LiCl/H ₂ O at a 25 μm diameter Pt microelectrode.	29

List of Figures - Continued

14. Experimental approach curves of 1 mM FcMeOH in 0.1 M LiCl/H ₂ O at insulating (blue) and conductive (red) substrates, generated with a microdisk electrode ($RG = 5.4$). Rate of approach 1.2 $\mu\text{m/s}$. A Pt electrode was biased and used as a conductive substrate.....	30
15. Boundaries of the model geometry.....	32
16. Schematic of the experiment and the definition of the coordinates 2.....	33
17. Comsol equation for the diffusion problem.....	35
18. Steady-state concentration profile at the SECM tip.....	37
19. An approach curve (dots) to an Au ₃₈ MPCs film taken with 1000 μM FcMeOH in LiCl/H ₂ O and the corresponding simulated theoretical curve (solid line).	38
20. Electron transport pathways in mixed DmFc-lipid monolayer deposited on a glass substrate. Curved arrows show electron “hopping”. Zigzag arrow shows physical diffusion to the surface. Red ellipses are the redox mediator in the bulk solution. ...	40
21. Surface pressure(π)-area(A) isotherms of saturated lipids with chain lengths of C10, C12, C14, C16, C18, and C20.....	42
22. Compression-expansion cycling of 6 saturated lipids with different chain lengths: DDPC (10:0), DLPC (12:0), DMPC (14:0), DPPC (16:0), DSPC (18:0), and DAPC (20:0). In the parenthesis are: the first number representing the number of the tail carbon atoms and the second number representing the number of the double bonds along the tail.	44
23. Compression-expansion cycling of unsaturated lipids. DOPC (18:1) and DOPE (18:2) isotherm cycles.....	45
24. Surface pressure(π)-area(A) isotherm of the dye molecule NBD-PE.....	46
25. Surface pressure(π)-area(A) isotherms of DMPE (14:0) with area/molecule 42.5 \AA^2 and DPPE (16:0) with area/molecule 29.6 \AA^2	46
26. LB deposition of DLPC (12:0) on a hydrophobic substrate ((CH ₃) ₂ Cl ₂ Si treated glass slip) at different surface pressures: 20, 30, 40, 45 mN/m. Successful transfer achieved only at 45 mN/m.	47
27. Deposition of DMPC (14:0) on a hydrophilic substrate at surface pressure of 25 mN/m.	48

List of Figures - Continued

28. Comparison of pressure(π)-area(A) isotherms of pure DMPC and 1 mol% NBD-PE/DMPC.	49
29. Fluorescence spectra of NBD-PE in chloroform solution.	50
30. UV-Vis absorption spectra of (a) 1 mol% NBD-PE/DMPC in chloroform, (b) NBD-PE monolayer on a silanized glass substrate, and (c) 1 mol% NBD-PE/DMPC monolayer on a silanized glass substrate.	50
31. Fluorescence of 1 mol% NBD-PE/DMPC monolayer taken with Nikon epi-fluorescence microscope.	51
32. Fluorescence recovery after photobleaching (FRAP) of 1 mol% NBD-PE/DMPC monolayer.	51
33. Cyclic voltammograms of only supporting (base) electrolytes: 0.1 M KCl and 0.1 M NaClO ₄ at a Pt electrode.	52
34. Cyclic voltammograms (CVs) of five redox couples: (a) 5 mM Ru(II)(CN) ₆ K ₄ /0.1 M NaClO ₄ in H ₂ O, (b) 1 mM Ru(II)(bpy) ₃ Cl ₂ /0.1 M KNO ₃ in H ₂ O, (c) 0.36 mM Mo(IV)(CN) ₈ K ₄ /0.1 M NaClO ₄ in H ₂ O, (d) 1 mM FcMeOH/0.1 M NaClO ₄ in H ₂ O, and (e) 5 mM DmFc (decamethylferrocene)/0.1 M TBA.ClO ₄ in DCE (dichloroethane). All CVs were taken at scan rate of 10 mV/s.	53
35. Decamethylferrocene (DmFc) structure. Neutral molecule with an iron atom in 2+ oxidation state.	54
36. Comparison of pressure(π)-area(A) isotherms of pure DMPC and 20 v/v % DmFc/DMPC monolayer.	55
37. AFM image of DMPC (14:0) lipid.	56
38. Scheme of SECM experiment with mixed DmFc-lipid monolayer.	57
39. An experimental approach curve (dots) to DmFc-DMPC monolayer. It fits well to the theoretical pure negative feedback (solid line).	58
40. Stability of contact angles on glass and ITO substrates. The glass substrate and ITO covered with 20 v/v % DmFc/DMPC monolayer.	60
41. Cyclic voltammograms at a bare ITO and at a modified ITO with a mixed DmFc-lipid monolayer. Electrolyte solution 0.1 M NaClO ₄ . Scan rate 0.01 V/s. The ITO was used as a macro-working electrode	61

List of Figures - Continued

42. Experimental design of a lipid monolayer modified ITO electrode. An electrolyte drop is placed on top of the monolayer, where the reference and the counter electrodes are immersed..... 62
43. Cyclic voltammogram of $\text{Mo(CN)}_8^{4-}/\text{Mo(CN)}_8^{3-}$ in $\text{NaClO}_4/\text{H}_2\text{O}$ at a bare and a lipid monolayer modified ITO. 63
44. Schematic of the studied gold hexalkanethiolate monolayer protected clusters. The normalized interparticle separation $d/2a$ was same for the first two samples A and B, which have on the same average core size, but different core size dispersity. With decreasing the core size to Au_{140} and Au_{38} MPCs the $d/2a$ value increases 65
45. SECM investigations of electron transport in a drop-cast AuMPCs film on a glass substrate. The arrows depict possible electron transfer pathways through the film. The SECM tip is immersed in an electrolyte solution containing a redox mediator (FcMeOH)..... 66
46. Differential pulse voltammetry (DPV) of 0.4 mM $\text{Au}_{38}(\text{SC}_6\text{H}_{13})_{24}$ in 0.1 M $\text{Bu}_4\text{NClO}_4/\text{CH}_2\text{Cl}_2$ at 0.4 mm Pt working electrode..... 68
47. Experimental approach curves (solid lines) to Au_{38} films, where normalized tip current is plotted as a function of tip-film distance at different redox mediator concentrations (from bottom to top: 1000, 100, 8, 6.5, 4.75, and 3 μM), and simulated approach curves (circles) generated with different values of the dimensionless conductivity Σ (from bottom to top: 0.001, 0.01, 0.1, 0.33) taken from Quinn's work³..... 70
48. Dimensionless conductivity Σ as a function of the inverse of the solution redox mediator concentration..... 72
49. Experimental approach curves to Au_{140} film, where normalized tip current is plotted as a function of tip-film distance at different redox mediator concentrations: 1000, 100, 8, 6.5, 4.75, and 3 μM . The theoretical curve (solid line) was calculated from equation 3.6. 73
50. Differential pulse voltammetry (DPV) of 0.4 mM $\text{Au}_{140}(\text{SC}_6\text{H}_{13})_{53}$ in 0.1 M $\text{Bu}_4\text{NClO}_4/\text{CH}_2\text{Cl}_2$ at 0.4 mm Pt working electrode and an Ag wire as a quasireference electrode. The potential of zero charge (PZC) is indicated in the figure. 74

List of Figures - Continued

51. Experimental approach curves to film A, where normalized tip current is plotted as a function of tip-film distance at different redox mediator concentrations (from bottom to top: 1000, 100, 8, 6.5, 4.75, and 3 μM), and the theoretical curve calculated from equation 3.6.....	76
52. Schematic of the electron transport between particles with different core size.....	77
53. Examples of experimental approach curves to film B, where normalized tip current is plotted as a function of tip-film distance at different redox mediator concentrations: 1000, 100, 8, 6.5, 4.75, and 3 μM and a theoretical curve calculated from equation 3.6.....	78
54. Electron transport through a gold nanoparticle film: (a) ordered lattice and (b) disordered lattice.....	79

CHAPTER I

INTRODUCTION

1.1 Scanning Electrochemical Microscope (SECM)

The aim of this thesis was to establish an experimental basis for exploration of electronic conductivity of different substrates, by using the scanning electrochemical microscope (SECM). The SECM was introduced in 1986 by Bard and coworkers as an instrument capable of examining electrochemistry at high resolution near interfaces⁴. The SECM can be used in a variety of ways in the study of heterogeneous and homogeneous reactions, as an imaging microscope. Depending on the kind of applications, different types of operational modes could be employed.

There are several modes of operation developed for the investigation of the local chemical properties of interfaces. A comprehensive review of all the techniques can be found elsewhere⁵. The SECM utilizes a position-controlled ultramicroelectrode, in either amperometric or potentiometric measurements. In the feedback amperometric mode the ultramicroelectrode (SECM tip) serves as a working electrode, where the current is recorded. When employing a potentiometric tip, no consumption of the analyte takes place and the SECM tip serves simply as a detector.

Figure 1 illustrates the wide ranging information that can be gained from the current of an amperometric SECM tip on different substrates under investigation. The arrows represent the flux of a redox-active species.

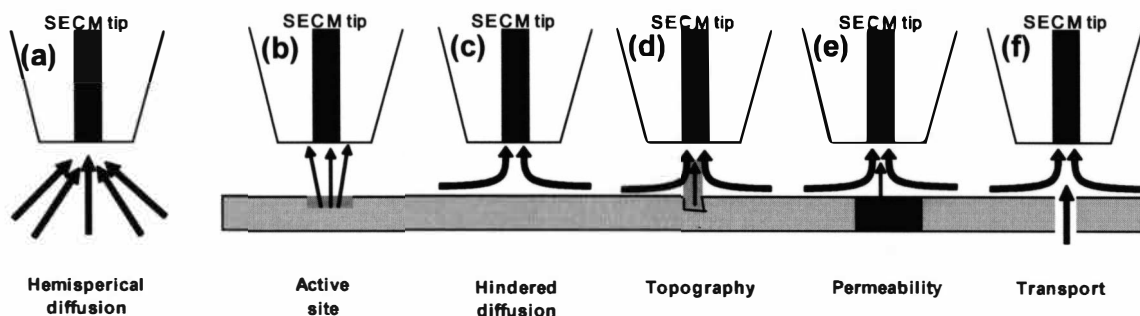


Figure 1 A selection of modes of operation of a SECM with an amperometric ultramicroelectrode tip.

In the current study SECM was used in a feedback mode. Detailed description of the operation of this technique is given in chapter II. Briefly, the tip perturbs locally an interfacial process at a substrate by electrolysis, when the SECM tip is brought close to the interface. When the tip is positioned at a relatively long distance from the target interface (Figure 1 (a)), it behaves as a conventional ultramicroelectrode⁶, i.e. a steady-state current is rapidly established due to the hemispherical diffusion of a redox-active species in the electrolyte solution where the tip is immersed.

When the tip is moved close to the interface (Figure 1 (b)), the tip generates a species by the redox process and it diffuses from the tip to the target interface. As this species undergoes a redox reaction at the interface, which converts it to original form, the product diffuses back to the tip. Thereby a feedback cycle is established and the current at the tip is enhanced (named 'positive feedback').

When the tip is brought close to an interface which is inert to the species involved in the electrode process (Figure 1 (c)), diffusion to the tip is hindered. The steady-state tip current decreases compared to the tip current far from the interface. The baseline response from these measurements is termed "negative feedback".

Instead of scanning of the tip only in the z-direction, topography of the interface can be obtained by scanning it in two-dimensional directions (Figure 1 (d)). Initially the SECM tip approaches the substrate in z-direction until the current is for example 80 % of that in the bulk solution. It is then scanned, at a fixed height in the x-y plane. The recorded current changes are related to a change in the tip-substrate separation. A theory relating the tip current with the distance has been developed⁷ and a map of the tip current as a function of the x-y tip position can be transformed into a two-dimensional height map which is a topographic image.

Amperometry is not limited to electron transfer reactions between a metal electrode and a redox moiety. Figure 1 (e) and (f) depicts permeability and direct transport of redox-active species as in a case of electron or ion transfer through an interface between two immiscible electrolyte solutions (ITIES) or through artificially constructed bilayer lipid membranes (BLMs). The electron transfer between redox species confined to two separate phases was investigated, where variable chain length phospholipids monolayers was adsorbed at the liquid/liquid interface⁸. The reaction between the tip-generated ZnPor^+ (zinc porphyrin) in a benzene phase and various aqueous phase reluctant was found to be dependent on the driving force (potential across the interface) and the thickness of the phospholipid monolayer at the interface. The electron transfer rate constants, measured in the presence of the phospholipid monolayer, were found to be lower than for the lipid-free interface. Bard and coworkers, also investigated the transport of I^- across BLMs using SECM approach curves⁹. They reported that the flux of I^- to the electrode tip was enhanced by addition of I_2 to the membrane forming solution, suggesting that this served as a carrier for I^- transport by formation of I^{3-} .

The type of probe electrode used in SECM depends on the particular process under investigation. Comprehensive reviews of ultramicroelectrode design, fabrication and characterization can be found elsewhere^{10, 11}. A variety of probes are available, for example submarine probes, sub-micron and nanometer scale probes, micro-ITIES probes, as well recent developed SECM-AFM probes^{12, 13}. The disk shaped microelectrode sealed in glass (typical diameter of 0.6-25 μm) is probably the most widely used and was also employed in this study. The voltammograms taken with a disk microelectrode are sigmoidal shaped at low scan rates under diffusion-controlled conditions. Another difference from the electrodes of conventional size is that these very small electrodes have a reduced double layer capacity (proportional to the electrode area) and small currents are generated during voltammetry. An advantage of the small currents is that voltage distortion of voltammograms, caused by iR drop, is greatly reduced.

1.2 Electron transport through thin organic films

In this work the SECM was used to probe the electron transport in lipid monolayers and films of monolayer protected gold nanoparticles. Understanding how electrons flow through organic matter is important in areas such as transfer in biological systems, fabricating microelectronic devices and sensors, and developing molecular electronics. One compelling feature of these organic films is that the electronic properties can be designed by independently varying three of the most important parameters of a solid – the site-site coupling, the lattice site charging energy, and the lattice symmetry.

Electronic coupling (site-site coupling)

Studies of electron transfer from a donor (D) to an acceptor (A) through a molecular bridge (B) in solution termed D-B-A assemblies provide information about the

relation between rates of electron transfer and molecular structure¹⁴⁻¹⁶. The rate of electron transfer generally depends exponentially on distance according to equation 1.1¹⁴:

$$k_{ET} = k_0 e^{-\beta d_{D,A}} \quad (1.1)$$

where k_{ET} is the electron transport rate constant, k_0 is a preexponential factor, β is a structure dependent attenuation factor that describes the decay of electronic coupling between D and A as the distance separating them increases, and $d_{D,A}$ is the distance between D and A.

The rate of the electron transfer (k_{ET})¹⁷ is proportional to the electronic coupling between the electronic wave functions of the donor and acceptor, $H_{D,A}^2$, (equation 1.2), and also to the Franck-Condon weighted density of states, $FCWD$, that describes the overlap of nuclear wave functions of the reactant and the product.

$$k_{ET} \propto H_{D,A}^2 (FCWD) \quad (1.2)$$

Equation 1.2 describes nonadiabatic electron transfer in molecular systems, where the contributions from the electronic and nuclear wave functions are explicitly separated.

From equations 1.1 and 1.2 one can predict that $H_{D,A}$ depends exponentially on the distance separating the electron donor and the electron acceptor because of the exponential drop-off of the electronic wave functions with distance.

Site charging energy

Charging energy, E_c , is the energy required to remove an electron from one isolated particle and add it to another isolated particle. It is inversely proportional to the total capacitance, C , between the particle and its surroundings¹⁸:

$$E_c = e^2 / C \quad (1.3)$$

e is the electronic charge.

To observe the unique discrete structure of a nanoparticle, the available thermal

energy, k_bT , must be smaller than e^2/C . At higher temperature, the thermal distribution of electrons in the particle masks the discrete structure. Modes coupled to electron transfer must be treated as quantum mechanical if the spacing between the vibrational levels is large compared to thermal energies¹⁷.

The nanoparticles are characterized by a size-dependent finite capacitance. The small capacitance of monolayer protected metal clusters (MPCs) arises from the combination of its small radius and the low dielectric of the surrounding monolayer. The concentric sphere capacitance model has been developed to account for the MPCs properties¹⁹. A capacitor formed from concentric spheres separated by a dielectric (monolayer) with thickness d has a capacitance, C , given by:

$$C = 4\pi\epsilon_0\epsilon(r/d)(r + d) \quad (1.4)$$

where ϵ_0 is the permittivity of free space, ϵ is the dielectric constant of the monolayer, and r is the core radius.

The cluster capacitance increases with core radius and decreases with monolayer chain length.

From equations 1.3 and 1.4, it can be seen that small nanoparticles (small r) have small capacitance ($C \propto r$) and high charging energy ($E_c \propto 1/C$). Hence, at room temperature usually $k_bT < E_c$ is fulfilled, because of the small capacitance of nanoparticles with size of few nanometers.

An electron can tunnel only between states of identical energy. Therefore, the charging energy is the barrier that has to be overcome before electrons can tunnel onto the particles. Electronic conductivity, σ , has been modeled by the Arrhenius equation²⁰:

$$\sigma = \sigma_0 \exp\left(-\frac{E_c}{k_bT}\right) \quad (1.5)$$

σ_0 is the preexponential constant.

From equations 1.4 and 1.5, it can be seen that the charging energy decreases with the particle size. This provides the theoretical framework explaining the core-size dependant conductivity, σ .

Disordering (lattice symmetry)

The role of defects on charge transport is critical for an understanding of the electrical response of a nanoparticle film. In a well ordered lattice the electronic coupling between neighboring nanoparticles occurs to a significant degree. It allows for facile electron transfer from one particle to another, resulting in the formation of delocalized states, as in a metal. When there is a local disorder (caused by large size distribution), the weak coupling due to discontinued lattice symmetry results in localizing of the states²¹ and the lattice may behave as an insulator (Anderson-type insulator)²².

In a polydisperse sample variation in core size leads to a variety of charge energies. The resulting energy barriers prevent unrestricted electron pathways over the particles²³.

1.3 Central hypothesis and structure of proposed research

Scanning electrochemical microscopy (SECM) is a powerful surface technique that can be used for investigation the activity and/or topography of an interface on a localized scale. The objectives of this study were to develop the SECM for investigating the lateral and long-range electron transport through thin organic films. The focus was on the electron transport in lipid monolayers and drop cast films of hexanethiolate gold monolayer protected clusters (AuMPCs).

In order to verify and explore this hypothesis of probing the electron transport in

the lipid monolayers and AuMPC films, first was developed an approach to use the SECM feedback mode for detection the electron transport in solid-state thin organic films (Chapter III). Compared with conventional electroanalytical methods to study conductivity of assemblies, SECM has a number of advantages such as being noninvasive, highly localized (small μm size tip), and not requiring the film to be externally biased. Characterization of the SECM tip shape (disk microelectrode) and quality, along with a simulation of a SECM experiment are given in Chapter III. The simulation couples lateral charge transport and surface reactions with species transport to the electrode surface.

Chapter IV provides the results from the formation, characterization, and SECM exploration of lipid monolayers. The transport processes at cell membranes are of vital biological importance and a lipid monolayer constitutes a useful model system for investigating electron transfer processes. The lipid monolayers were formed by using the Langmuir-Blodgett technique. The quality and stability of lipid monolayers were characterized by fluorescence spectroscopy and microscopy, contact angle, and electrochemistry using a monolayer modified ITO (indium tin oxide) electrode. Electroactive species (decamethylferrocene) were added to the lipid matrix in order to explore the electronic conductivity through the monolayer using SECM. In the SECM measurement, the monolayer electron transport was not detected. The monolayer quality turned out to be not suitable for studying the electron transport.

Finally in Chapter V are discussions on size-dependant conductivity and disordering effect of drop cast films of gold monolayer protected cluster (MPC) with different core-sizes (1-3 nm diameters). Au MPCs of this size range are of particular interest because they represent the bulk-to-molecule transition region where electronic

band energetics yield to quantum confinement effects and discrete electronic states emerge. In the SECM measurement, the film conductivity was extracted from the feedback currents collected as a function of the tip and the MPC film distance using different bulk concentrations of a redox mediator (ferrocene methanol). The conductivity appears to be dependant on the MPC core-size, but the difference in their core-size distributions was found to have a pronounced effect on the electron transport in the films.

CHAPTER II

EXPERIMENTAL SECTION

2.1 Materials

Lipids

The saturated lipids investigated in the current study were:

1,2-didecanoyl-sn-glycero-3-phosphocholine (DDPC): 10:0 PC

1,2-dilauroyl-sn-glycero-3-phosphocholine (DLPC): 12:0 PC

1,2-dimyristoyl-sn-glycero-3-phosphocholine (DMPC): 14:0 PC

1,2-dipalmitoyl-sn-glycero-3-phosphocholine (DPPC): 16:0 PC

1,2-distearoyl-sn-glycero-3-phosphocholine (DSPC): 18:0 PC

1,2-diarachidoyl-sn-glycero-3-phosphocholine (DAPC): 20:0 PC

All the lipids have the same head group, PC, and differ only in the length of their tails having different number of carbon atoms. For example 10:0 PC (the first lipid in the list) means that this lipid has 10 carbon atoms long tail and 0 double bonds along the tail.

The two unsaturated lipids below have the same head group, PC, as the saturated lipids, but one and two double bonds respectively notated as 18:1 PC and 18:2 PC.

1,2-Dioleoyl-sn-glycero-3-phosphocholine (DOPC): 18:1 PC

1,2-Dilinoleoyl-sn-glycero-3-phosphoethanolamine (DOPE): 18:2 PE

For the fluorescence investigation, a dye molecule named:

1,2-Dipalmitoyl-sn-glycero-3-phosphoethanolamine-N-(7-nitro-2-1,3-benzoxadiazol-4-yl): 16:0 NBD-PE was used and it was a head group tagged lipid.

Additionally, the two saturated lipids with PE heads groups were:

1,2-Dimyristoyl-sn-glycero-3-phosphoethanolamine (DMPE): 14:0 PE

1,2-Dipalmitoyl-sn-glycero-3-phosphoethanolamine (DPPE): 16:0 PE

All the lipids were purchased from Avanti Polar Lipids, Inc.

Electrochemical materials

The electroactive species (1) and the supporting electrolytes (2), all purchased from Sigma-Aldrich, Co., were:

(1) decamethylferrocene (DmFc) also called bis(pentamethylcyclopentadienyl) iron(II) was sublimed before use; potassium hexacyanoruthenate(II) ($\text{K}_4\text{Ru}(\text{CN})_6$); tris(2,2'-bipyridyl)dichlororuthenium(II) hexahydrate ($\text{Ru}(\text{bpy})_3\text{Cl}_2 \cdot 6\text{H}_2\text{O}$); potassium octacyanomolybdate(IV) hydrate ($\text{K}_4\text{Mo}(\text{CN})_8 \cdot \text{H}_2\text{O}$); and ferrocenemethanol (FcMeOH).

(2) potassium chloride (KCl); sodium perchlorate (NaClO_4); potassium nitrate (KNO_3); and tetrabutyl ammonium perchlorate (Bu_4NClO_4);

Materials used for gold monolayer protected clusters (AuMPCs) synthesis

All the compounds used for AuMPCs synthesis were purchased from Sigma-Aldrich, Co. The quantities used were as follows:

3.1 g $\text{HAuCl}_4 \cdot \text{H}_2\text{O}$ (hydrogen tetrachloroaurate trihydrate) in 200 mL water

4.0 g $\text{N}(\text{C}_8\text{H}_{17})_4\text{Br}$ (tetraoctylammonium bromide) in 200 mL toluene

3.5 mL hexanethiol for 1:3 gold to thiol ratio and 1.2 mL for 1:1 gold to thiol ratio

3.8 g NaBH_4 (sodium borohydride) in 60 mL water

2.2 Langmuir-Blodgett trough

The Langmuir-Blodgett trough (Nima Technology, model 612D) shown in Figure 2 consists of a PTFE trough $20 \times 30 \times 0.8 \text{ cm}^3$ with 2 mechanically coupled barriers, a dipping well $10 \times 2 \times 10 \text{ cm}^3$ deep, a dipper mechanism with a stroke of 75 mm, and a Wilhelmy plate surface pressure sensor.

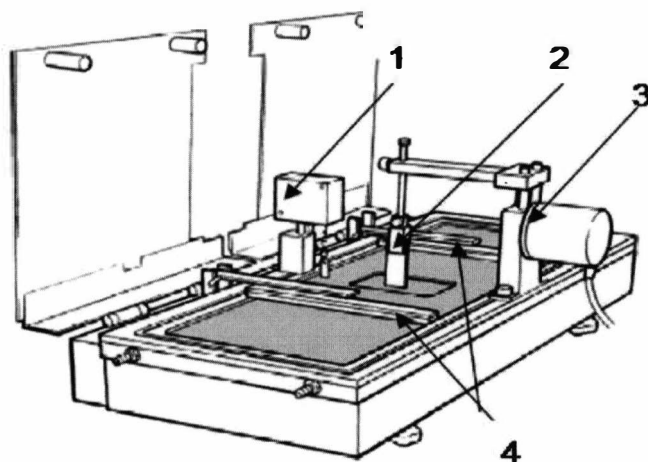


Figure 2 Langmuir-Blodgett trough. 1-Surface tension sensor, 2-Substrate for deposition, 3- Dipper mechanism, 4-Barriers for monolayer compression and expansion.

In a typical experiment, a lipid monolayer was formed at the air/water interface by spreading 50 μL of chloroform solution containing the lipid of interest (1 mM) onto the aqueous subphase. The temperature was maintained at 20°C by connecting of the trough to thermostatic circulating water. The solvent was allowed to evaporate for 20-30 minutes and the barriers were moved inward (25 cm^2/min) and the surface pressure (π) was recorded as a function of the area (A). Several compression-expansion cycles were conducted before the monolayer was transferred by Langmuir-Blodgett technique (Figure 3) at 6 mm/s speed. The transferring process usually involved two substrates that were generated by clipping them together before being dipped into the trough. In this manner only one side of the substrate was coated with the monolayer, and two samples were made using the same conditions. The transferred monolayer was stored in a desiccator until further use.

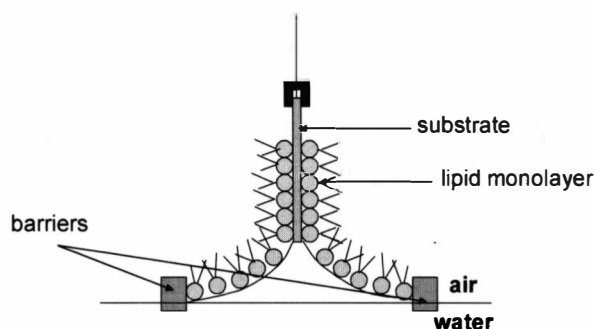


Figure 3 Langmuir-Blodgett technique for monolayer transfer.

Figure 3 Langmuir-Blodgett technique for monolayer transfer. Figure 3 shows a monolayer deposition on a hydrophilic substrate (e.g. glass slide). The substrate must be first lowered into the water subphase prior to spreading and compressing the monolayer. Pulling up of the substrate results in the sticking of the hydrophilic heads of the amphiphilic lipid on the substrate. The barriers move automatically inward to keep a constant surface pressure during the deposition process.

2.3 Fluorescence microscopy

An epi-fluorescence (reflected light fluorescence) microscope Nikon, E600 (Mager Scientific, Inc.) is shown in Figure 4. It was used for observing dye containing monolayers and for the monolayer photobleaching. The light source was a mercury lamp and the epi-fluorescence filter (420-620 nm) was exciter HQ 480-440 and emitter HQ 535-550. A monolayer was photobleached for 30 seconds through a 40x objective and the recovery of the bleached spot was observed through a 10x objective.

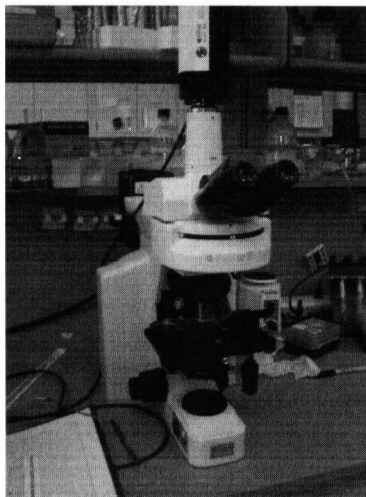


Figure 4 Epi-flourescence microscope Nikon Eclipse.

2.4 UV-VIS and fluorecence spectrometers

Spectrophotometer PerkinElmer, Lambada 40 and spectrofluorimeter PerkinElmer, LS50B were used for the optical measurements. Standard cuvettes were used for the liquid samples. For the deposited layers the substrate was cut to a size that fits into the cuvette holder.

2.5 Contact angle measuring instrument

The drop shape analysis instrument (Kruss USA/DSA, DSA10-Mk2) consists of a computer controlled liquid dispensing, a temperature controlled table, a video system, and optics. Typically a 10 μL drop of ultrapure water was dispensed close to the surface of interest using a syringe needle of 0.5 mm diameter. The needle was lifted up from the drop and video of the contact angle with time is recorded every 8th second for approximately 10 minutes. The Young-Laplace method²⁴ was used for fitting and

calculating the contact angles of static drops.

2.6 Electrochemistry with modified ITO

The size of a conductive ITO slide was 25x75x1.1 mm with resistance of $10 \pm 5 \Omega$. It is commercially available from Delta Technologies (part # CB-50IN-S111) and was cleaned in 20% ethanolamine: water (w/w), heated up at 80°C for 30 minutes under sonication. A copper wire was pasted to the edge of the ITO slide using silver epoxy, which was dried at 80°C for 90 min. The ITO was modified with a monolayer of interest and used as a working electrode. The monolayer transfer was carried out by vertical dipping of the ITO in the Langmuir-Blodgett trough. A drop of aqueous electrolyte solution containing 0.36 mM $\text{Mo}(\text{CN})_8^{4-}$ in 0.1 M NaClO_4 was placed on top of the monolayer (either pure lipid or mixed decamethylferrocene-lipid). The reference and counter electrodes (RE and CE) were immersed in the drop. RE was Ag/AgCl and CE was 0.4 mm Pt wire. This system was examined by cyclic voltammetry and a series of current-potential voltammograms were recorded.

2.7 Scanning Electrochemical Microscopy (SECM)

The basic components of the scanning electrochemical microscope (CH-Instruments, model 900B) are shown in Figure 5 – an XYZ tip nanopositioner (stepper and piezo controller), an electrochemical cell, a bipotentiostat with a potential range ± 10 V and a current range ± 10 mA (low current measurability of 1 pA), and a high-resolution data acquisition system. The stepper motor can travel up to 2.5 cm with a resolution of 100 nm and the piezo motor can travel up to 85 μm with a resolution of 1.6 nm. However the stepper motor has backlash of 2-3 μm and when the scan direction is changed the

motor may not move for the first 2-3 μm , which would cause uncertainty in positioning.

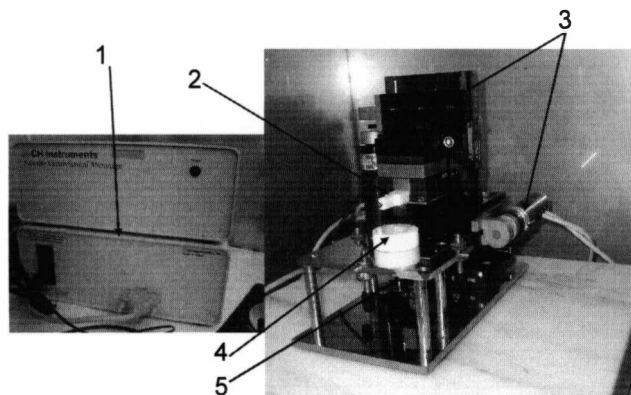


Figure 5 SECM apparatus. 1-Bipotentiostat & data acquisition, 2-Tip holder, 3-XYZ tip positioners, 4-Electrochemical cell, 5-Substrate electrode

The electrochemical cell consists of 4 electrodes – reference, counter (0.5 mm Pt wire, and two working electrodes (a 3 mm Pt disk substrate electrode and a tip electrode).

In the current study a 2 electrode system was employed for investigating AuMPCs substrate. The reference and counter electrode leads were shortened to clip a 0.5 mm Ag wire (quasi-reference electrode) and a 25 μm diameter Pt tip electrode was used as a working electrode.

The instrument also offers a wide range of conventional electrochemical techniques; for example, sweep technique of cyclic voltammetry (CV) was used for the formal potential investigation of the redox mediators. The CV was employed with 3 electrode system, where the reference electrode was non-polarizable Ag/AgCl, the counter electrode was 0.5 mm diameter Pt wire and the working electrode was a 25 μm diameter Pt SECM tip (disk microelectrode).

Three drops of 100 μL chloroform solution containing 0.3 mg/mL AuMPCs in chloroform solution were cast on a precleaned glass slip and air dried. An aqueous drop

of 40 μL containing FcMeOH and 0.1 M LiCl was then placed on top of the AuMPCs film sample. The SECM tip along with the Ag wire was immersed in the drop and the sample film was examined by the SECM.

The SECM feedback experiments of AuMPCs films were performed by starting with the highest concentration of the redox mediator FcMeOH (1000 μM), in order to obtain a pure negative feedback for the exact tip-substrate distance determination. CVs were recorded far from the substrate for the electrode radius evaluation. The tip was biased at 0.35 V (vs AgQRE) where the diffusion controlled oxidation current for FcMeOH and an approach curve using probe approach curve technique was recorded. The rate of approach was maintained by the stepper motor at 1.2 $\mu\text{m/s}$. The tip was then retracted 150 μm and the electrolyte drop was replaced with a pipette by another drop containing lower FcMeOH concentration. An approach curve for this concentration of mediator was measured, followed again by tip retraction. This was repeated for 100, 8, 6.5, 4.75, and 3 μM FcMeOH concentrations with constant 0.1 M LiCl as a supporting electrolyte. All approach curves were corrected for the background response of 1 pA.

2.8 Disk microelectrode fabrication

There are a variety of methods for fabrication of different types of SECM tip electrodes²⁵⁻²⁸. The disk shaped electrode is most widely used. There are commercially available tips made of Pt wire with diameter of 10 μm . For our needs a tip with Pt wire diameter of 25 μm was fabricated. The borosilicate capillary tube in Figure 6A with outer diameter 2 mm and inner diameter 1 mm was cleaned in piranha solution (3 (H_2SO_4): 1(H_2O_2)). One of its ends was sealed by slowly rotation of the tube in a torch flame (the sealed tube is shown in Figure 6B).

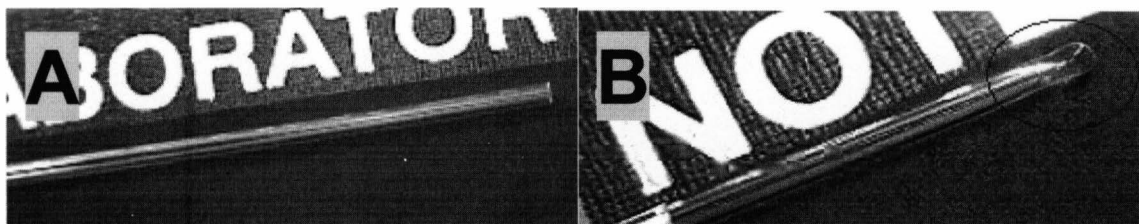


Figure 6 A: Clean borosilicate capillary tube and B: torch sealed capillary tube.

A 25 μm diameter Pt wire (1.5 cm in length) was straightened by rolling it on a glossy paper and was introduced in the sealed tube (in the crack of the cone). The open end of the capillary was connected to vacuum for 30 minutes before the next step, in order to remove air inside the tube. The next phase shown in Figure 7 was sealing of the tube onto the Pt wire by Ni-Cr resistor coil (5 mm inner diameter). The coil was connected to a power supply and potential of 7 V (14 A) was applied for 10 min. The capillary with the wire was about 4 mm inside the coil initially and about 6 mm inside the coil for extra 5 minutes at 8 V (17 A).

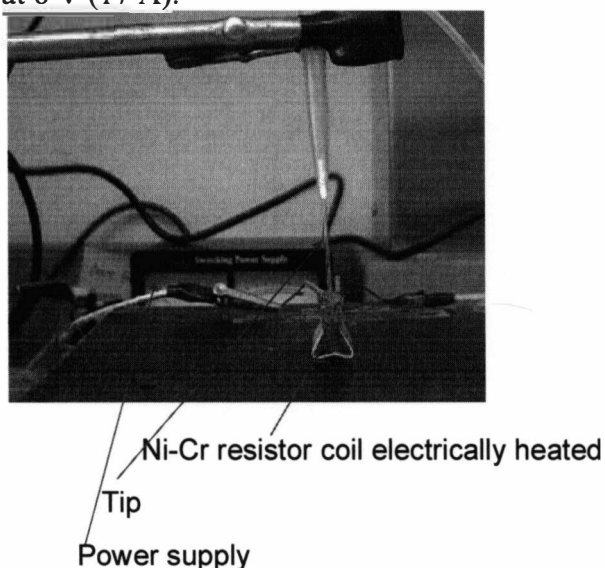


Figure 7 The capillary is aligned with a resistor coil.

The alignment of the wire in the capillary (Figure 8) was checked with microscope (Nikon, Mager Scientific, Inc.). No air pocket or bubble was seen, which could potentially cause problems after polishing.

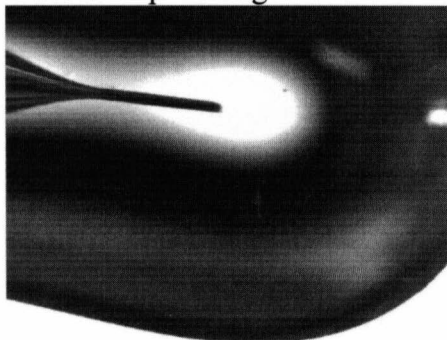


Figure 8 Sealed 25 μm diameter Pt wire in a capillary tube resulted from coil heating.

Figure 9 shows the injection of conductive silver epoxy into the capillary in order to make an electrical contact between the Pt wire and the lead wire (Cu 30AWG wire). The prepared electrode in this way was put in an oven overnight at 120°C for drying of the epoxy.

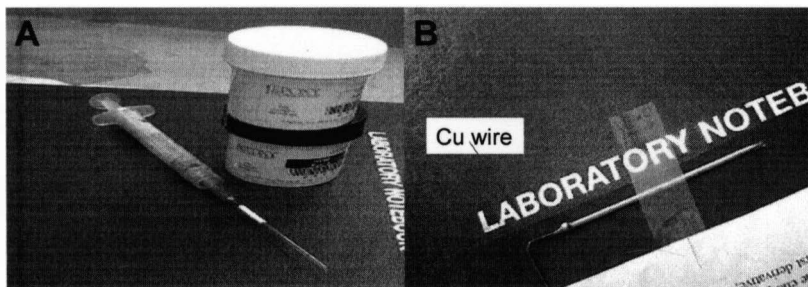


Figure 9 A: Injection of conductive silver epoxy around the Pt wire and B: Introduced Cu wire in the capillary tube for electrical contact with the Pt wire.

The final step consists of polishing of the tip by using different sized sand paper (grid size 240 and 1200) and alumina powder (particle size 1, 0.3, and 0.05 μm). Gradual

decrease of the particle size was required to achieve the finest smooth surface. The tip was polished in a cone shape until the ratio between the overall glass radius and the wire radius was 7.5 and later 5.4 (an important tip parameter termed R_G). Figure 10A displays unsuccessful polishing due to miscentered wire. This tip was not used, because the diffusion of electroactive species to the Pt wire would be complicated and undefined. Figure 10B shows the final image of the fabricated SECM tip used in this study.

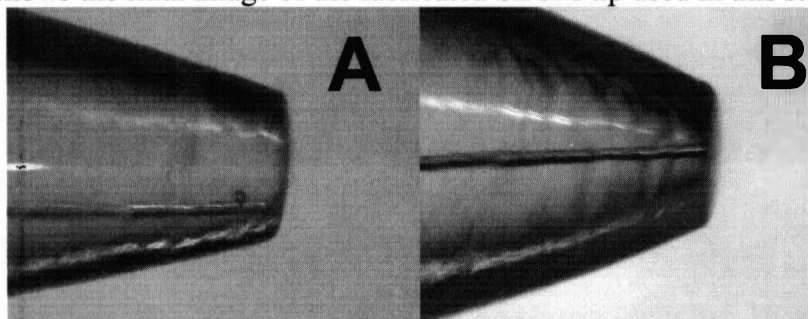


Figure 10 Polished SECM tip. A: Example of a mispolished tip and B: Image of a successfully polished tip.

2.9 AuMPCs synthesis

The synthesis of alkanethiolate gold monolayer protected clusters (AuMPCs) was conducted according to the well known Brust two-phase procedure²⁹. Initially, Au in a form of water-soluble chloraurate salt ($\text{HAuCl}_4 \cdot \text{H}_2\text{O}$) was extracted in toluene ($\text{C}_6\text{H}_5\text{CH}_3$) using tetraoctylammonium bromide ($\text{N}(\text{C}_8\text{H}_{17})_4\text{Br}$). Addition of hexanethiol ($\text{C}_6\text{H}_{13}\text{SH}$) to the toluene solution led to formation of gold polymer $(\text{--Au}^{\text{I}}\text{SC}_6\text{H}_{13}\text{--})_n$, which was followed by further gold reduction with sodium borohydride (NaBH_4). The resulting Au^0 MPCs have a 1-5 nm range of core diameters. The reactions involved are:





The exact mechanism of AuMPCs formation is not well understood, but it is related to a nucleation-growth-passivation process and it was studied by Murray's group³⁰. MPCs core sizes are function of thiol to gold mole ratio, speed of the reductant addition and the reduction temperature. Lowered temperature and presence of more thiol passivates the gold growth faster and results in smaller and relatively monodisperse AuMPCs. Additionally, fractionizing was achieved by size-dependent solubility of the AuMPCs in solvents such as ethanol and acetone. Ethanol soluble part was a small portion of $\text{Au}_{38}(\text{C}_6\text{H}_{13}\text{S})_{24}$ and the precipitate was further dissolved in acetone. The solid part contained a mixture of bigger sizes and the filtrate was $\text{Au}_{140}(\text{SC}_6\text{H}_{13})_{53}$. For $\text{Au}_{38}(\text{SC}_6\text{H}_{13})_{24}$, $\text{Au}_{140}(\text{SC}_6\text{H}_{13})_{53}$ and AuMPCs (2.22-3.16 nm) samples a ratio (gold:thiol) of 1:3 was used. Another sample, AuMPCs (1.69-3.80 nm), was prepared in the same manner, but by using a ratio (gold:thiol) of 1:1. Samples AuMPCs (2.22-3.16 nm) and AuMPCs (1.69-3.80 nm) will be referred as sample A and sample B. They were isolated using solvent (hexane) and non-solvent (ethanol) mixture. The first precipitation from sample A and the second precipitation from sample B were isolated and used for further investigation.

After the AuMPCs isolation, the samples were characterized by UV-VIS and TEM. Figure 11 shows UV-VIS spectra of the four examined samples Au_{38} , Au_{140} , sample A and sample B.

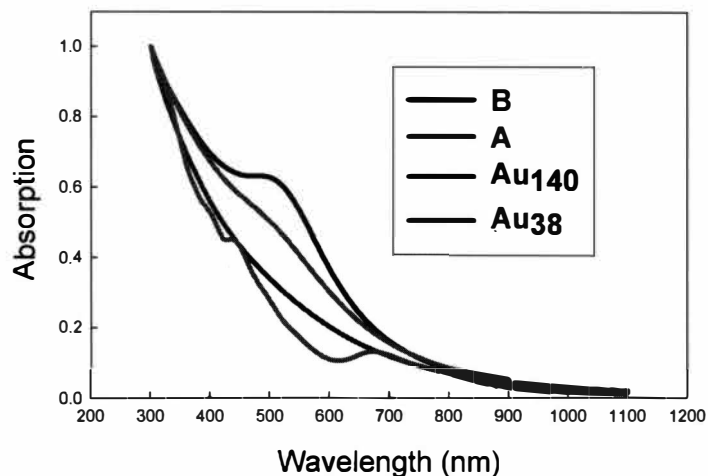


Figure 11 UV-VIS spectra of AuMPCs in dichloromethane. The spectra are normalized to unity absorbance at 300 nm.

Samples A and B exhibit UV absorption feature with a surface plasmon (SP) band at ~ 520 nm. Consistent with the literature³⁰ the SP band decreases in intensity with decreasing gold cluster size. Despite the similar average size of both samples, the presence of big particles in sample B (polydisperse) leads to higher intensity of the SP than sample A. The SP was undetectable for Au₁₄₀, which is an indication of the loss of bulk character. Moreover, the last smallest cluster (Au₃₈) demonstrates molecule-like properties and transitions by displaying a stepwise structure, two peaks at ~ 430 and ~ 660 nm, that is typical for a small core size³¹.

The core size of the four examined samples was characterized by TEM (Figure 12). The particle size distributions are displayed as insets.

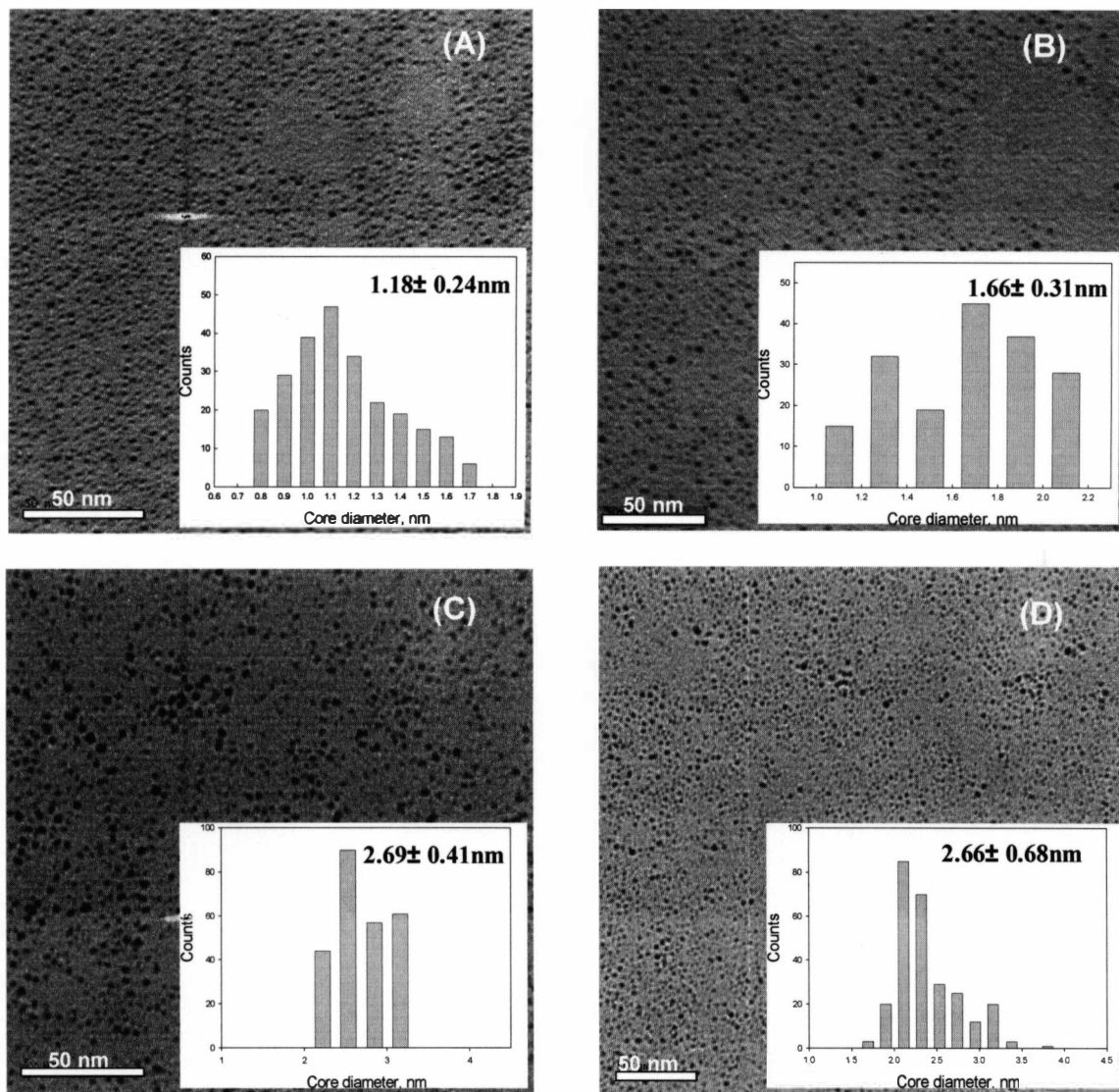


Figure 12 TEM images of (A) $\text{Au}_{38}(\text{SC}_6\text{H}_{13})_{24}$; (B) $\text{Au}_{140}(\text{SC}_6\text{H}_{13})_{53}$; (C) AuMPCs (1:3); (D) AuMPCs (1:1). Insets show the histograms of the core diameter, where the standard deviations from the mean is displayed.

2.10 Electrochemistry of AuMPCs

A step technique of differential pulse voltammetry (DPV) was employed with AuMPCs electrolyte solutions. Typically, the solutions contained 0.2-0.4 mM AuMPCs

and 0.1 M Bu₄NClO₄ dissolved in dichloromethane (CH₂Cl₂) and it was purged for oxygen removal 10-15 minutes with nitrogen in a well sealed vial. The electrode was prepared by sealing of three metal wires in epoxy so that only their ends were exposed to the solution. The reference electrode was Ag wire of a 0.5 mm diameter, the counter electrode Pt wire of a 2 mm diameter, and the working disk electrode Pt wire of a 0.4 mm diameter. First, an open circuit potential-time (OCPT) voltammogram was recorded, in order to extract information about the rest potential of AuMPCs solution. The rest potentials were used to calculate the ratio of the AuMPCs core charge states, in particular Au₃₈(SC₆H₁₃)₂₄ and Au₁₄₀(SC₆H₁₃)₅₃ samples based on the Nernst equation:

$$E_{rest} - E^{0'} = 0.059 \log \frac{[AuMPC^{z+1}]}{[AuMPC^z]} \quad (2.3)$$

where E_{rest} is the potential that flows between the working and reference electrodes immersed in a solution of interest without applying of an external current (given by OCPT), $E^{0'}$ is the pseudo-formal potential (versus potential of zero charge, PZC) of AuMPCs for one-electron charging step (given by DPV), and z is the core charge of AuMPCs (given by DPV). For example the Au₁₄₀(C₆H₁₃S)₅₃ sample had $E_{rest} = 0.002$ V and $E^{0'}(AuMPC^+/AuMPC^0) = 0.0917$ V (vs PZC), hence the ratio of $[AuMPC^+]/[AuMPC^0] = 0.03$ and the sample was mainly with uncharged gold cores. Au₃₈(SC₆H₁₃)₂₄ sample had $E_{rest} = 0.019$ V and the ratio of $[AuMPC^+]/[AuMPC^0] = 0.00016$, showing also the domination of uncharged gold cores.

2.11 Transmission electron microscope (TEM)

Samples for TEM were prepared by drop casting one drop of a ~1 mg/mL cluster solution in dichloromethane onto standard carbon coated (200-300 Å) Formvar films on copper grids (400 mesh) and drying in air for 10 min. Phase-contrast images of the particles were obtained with a JEOL-JEM 1230 electron microscope at 80 keV. Two typical regions of each sample were obtained at 400,000X and 600,000X. Size distributions of the gold cores were measured from enlarged TEM image photographs for at least 250 individual cluster core images.

CHAPTER III

DEVELOPMENT OF SCANNING ELECTROCHEMICAL MICROSCOPY (SECM)

The use of SECM eliminates many typical sources of experimental errors such as the effects of the resistive potential drop in solution, charging current, and enables analytical measurements to be performed at the interfacial region. The SECM (this abbreviation is used for the device, i.e., microscope and the technique - microscopy) utilizes a microelectrode tip, which is the main factor determining its great spatial resolution. The well defined steady-state current, relatively immune to convection at the microelectrode tip, allows the tip to be brought close to a surface, where the surface chemical reactivity can be probed.

In the current study SECM was used in feedback mode. Instead of scanning of the tip in three dimensions, only the *z*-direction is used. In the feedback mode the microelectrode tip serves as a working electrode. The tip potential is controlled versus a reference electrode and the current flows between the tip and a counter electrode. The sample, also referred to as a substrate, may be biased and employed as a second working electrode. The electrodes are immersed in a solution containing redox mediator, for example oxidisable species, *R*, at a concentration c^b and with a diffusion coefficient, *D*. When a sufficiently positive potential is applied to the tip, oxidation of *R* to species *O* occurs:



at a rate governed by the diffusion of *R* to the microelectrode tip.

When the tip is far from the substrate, greater than a few tip diameters, the steady-state current, i_{ss} , flows and is expressed by the well-known equation for the disk microelectrodes³²:

$$i_{ss} = 4naFDc^b \quad (3.2)$$

where n is the number of electrons transferred, a is the radius of the electrode, F , Faraday constant, D , diffusion coefficient of the electroactive species, and c^b is the concentration of the electroactive species.

When the tip is within a few tip diameters to a conductive substrate, the O species formed in reaction 3.1 diffuses to the substrate and may be reduced back to R as a result of the interfacial reaction between O and the substrate. As a result, an additional flux of R to the tip is produced, increasing the tip current - the smaller the tip-substrate distance, the higher the tip current. This is called "positive feedback". Clearly, the current at the tip is a function of its distance from the substrate and also the rates of reactions that occur at the substrate to generate species that are oxidized or reduced at the tip.

On the other hand, when the SECM tip approaches an insulating substrate, the O species formed in reaction 3.1 diffuses to the substrate, but can not react with the surface. A blocked diffusion of R occurs and the tip current decreases. As a result of the close proximity of the tip and the substrate, the rate of reaction 3.1 decreases. This phenomenon is termed "negative feedback".

The magnitude of the positive (negative) feedback is determined by the rate of the mediator regeneration at the tip substrate. Therefore, the analysis of the experimental positive (negative) feedback approach curve will provide information about the electron transfer kinetics at the substrate³³.

3.1 Characterization of a fabricated SECM tip

A disk-shaped microelectrode tip was fabricated in house to be used in SECM measurements (see experimental section). The electrode size is the main parameter

determining the resolution in SECM^{34, 35}. The small size allows for building up a large diffusion layer (with respect to the electrode area, the diffusion layer thickness taken as $2(Dt)^{1/2}$) in a short time and the current at any microelectrode achieves a steady state. This feature is important since kinetic measurements can be carried out at steady-state conditions³⁶. Small disk-shaped electrodes have the advantage of a quite reproducible surface, and a well-established theory for mass transport and kinetics is available for this type of geometry^{7, 37, 38}.

The SECM tip was first tested for a good electrical connection by a cyclic voltammogram (CV) with a well-defined reversible redox couple such as FcMeOH. A typical CV is shown in Figure 13. The radius of the SECM tip was determined by the microelectrode equation 3.2 ($i_{ss} = 4naFDc^b$). The obtained electrochemical radius of 15 μm is sometimes larger than the nominal 12.5 μm radius of the Pt wire used for the tip fabrication. The reasons could be that the Pt wire is slightly tilted in the insulating glass tube during sealing or small deviation in the thickness of the wire. Since the tip current is directly related to the tip size (equation 3.2), the electrode size was evaluated after every polishing by CV.

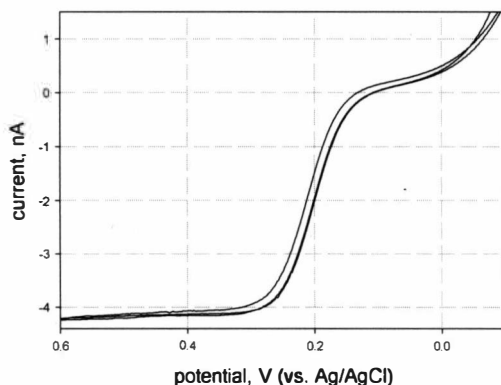


Figure 13 Cyclic voltammogram of 1mM FcMeOH in 0.1 M LiCl/H₂O at a 25 μ m diameter Pt microelectrode.

The SECM is typically used for characterization of an unknown substrate. However, it can also be used for characterization of the tip shape and quality for a well-defined substrate³⁹. An important characteristic of the SECM tip is the ratio of the tip radius that includes the insulating glass sheath to that of the metal wire radius known as R_G ratio ($R_G = R_{glass}/a$). Using a tip with small R_G (<10) value allows for obtaining a closer tip-substrate distance. The R_G effect can be significant especially in experiments with an insulating substrate³⁷. This effect is explained in terms of hindered diffusion of a redox mediator from the bulk solution to the tip⁴⁰. The theoretical dimensionless current/distance curves for steady state (time independent) processes have been obtained numerically for different R_G values. The zero tip-substrate separation is essential for any quantitative SECM measurement. It can be determined by fitting the experimental current/distance curves (termed approach curves) to the theoretical curves.

Figure 14 shows experimental approach curves, at insulating and conductive substrates respectively, generated with the fabricated SECM tip. The experimental current values (i_{tip}) and distances from the scan initial point (d_{exp}) were normalized

according to equations 3.3 and 3.4 below to make them compatible with the theoretical equations for conductive (3.5) and insulating substrates (3.6).

$$i_{Tip} \rightarrow I = i_{Tip} / i_{Tip,\infty} \quad (3.3)$$

$$d_{exp} \rightarrow L = d/a = (d_0 - d_{exp})/a \quad (3.4)$$

$$I = 0.72535 + 0.75649/L + 0.26115 \exp(1.60893/L) \quad (3.5)$$

$$I = 1/[0.48066 + 1.20599/L + 0.51815 \exp(2.09981/L)] \quad (3.6)$$

where I is the normalized current, $i_{Tip,\infty}$ is the steady state current in the bulk solution far from the substrate, L is the normalized tip-substrate distance, d_0 is the distance from the scan first point to the substrate surface (the last recorded distance), and the coefficients (equations 3.5 and 3.6) are numerical values given from the simulation in the work of Amphlett and Denuault⁴⁰.

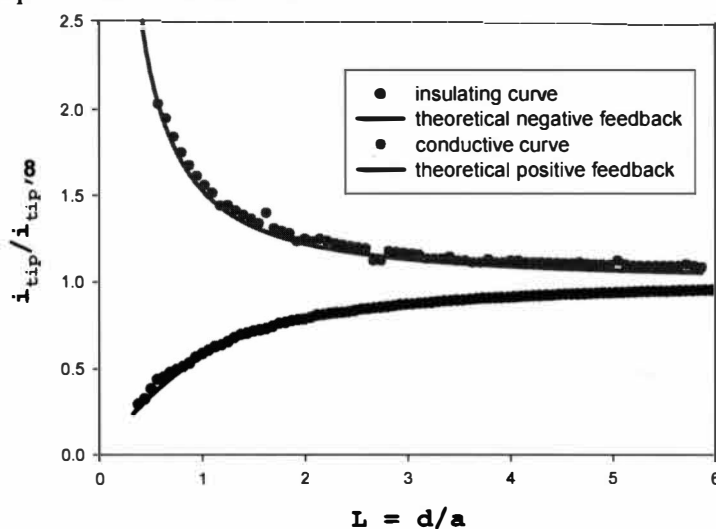


Figure 14 Experimental approach curves of 1 mM FcMeOH in 0.1 M LiCl/H₂O at insulating (blue) and conductive (red) substrates, generated with a microdisk electrode ($R_G = 5.4$). Rate of approach 1.2 $\mu\text{m/s}$. A Pt electrode was biased and used as a conductive substrate.

The insulating and conductive approach curves in Figure 14 were in agreement with the theoretical fitting, which suggests a good quality of the fabricated SECM tip.

3.2 Simulation of a SECM experiment

The commercial simulation package Comsol Multiphysics (based on finite element method) connected to MatLab was used to simulate an experiment involving electronic conductivity in thin films of gold monolayer protected particles. The simulation includes three steps: (1) solving the diffusion problem at a disk microelectrode; (2) solving the charge transport in the film; and (3) solving the electron transfer reaction problem between the solution redox couple and the nanoparticle film. Repeating these three steps at varied electrode-substrate distances would give the mass balance at different points in the system simulating the tip moving in a typical SECM experiment. Simply, this model couples lateral charge transport and surface reactions with species transport to the electrode surface.

Step (1) and (3) were solved successfully. Step (1) was solved using Amemiya's procedure⁴¹. Step (2) (related to the lateral charge transport), however, requires use of the weak form of partial differential equations (PDE), which is a much more involved process. Therefore it was left for future investigations. Step (3), which is related the coupling of the substrate reactions to mass balance in the bulk also required using the weak form, but an equation that is already built into Comsol Multiphysics was used⁴². This model, while not complete, could serve as a good starting point for further development of the lateral charge transport. The present model clearly simulates the case when the SECM tip is used to approach an insulating substrate, i.e. there is no reaction involving electron transport at the substrate.

A Comsol model consists of geometry (Figure 15), boundary conditions, material properties and PDE system.

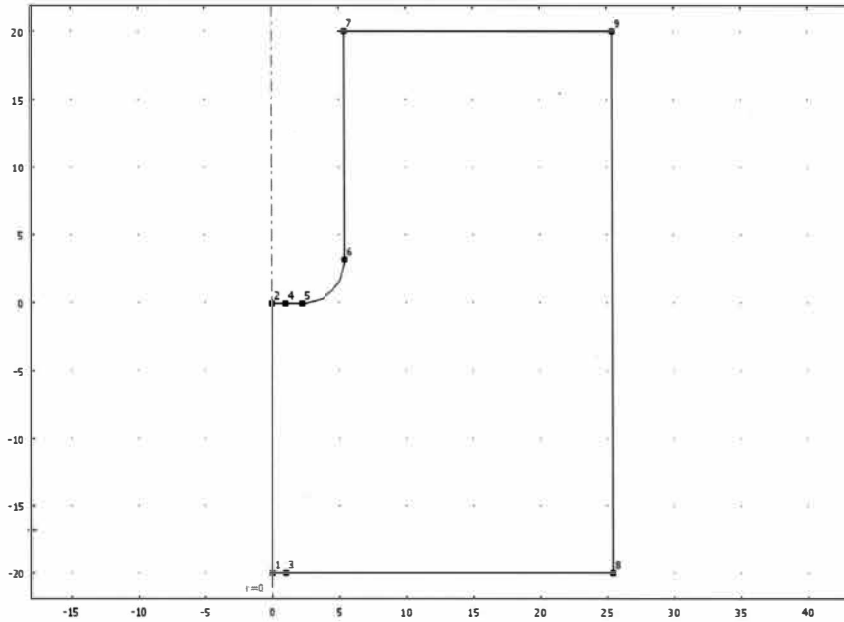


Figure 15 Boundaries of the model geometry.

The boundary defined between points 2 and 4 in Figure 15 represents the electrode surface. The substrate surface is illustrated between points 1 and 8. The rest of the boundaries are described as follows:

points 1-2: the distance between the electrode and the substrate

points 1-3: a part of the substrate immediately accessible under the electrode

points 4-5-6: insulating glass sheath of the SECM tip electrode

points 6-7: the outer edge of the SECM tip

points 7-9 and 9-8: physical boundaries of the container where the electrode is immersed

All boundaries are drawn using axial symmetry 2D (radial coordinates). Only the

substrate (1-3-8) was drawn in plane 2D.

The work of Quinn's group² was used for a schematic of the experiment and the definition of the coordinates shown in Figure 16. In their work, the effect of back-diffusion (behind the plane of microelectrode) based on the theory given by Denuaut and Amphlett⁴⁰, has been taken into account. The typical boundary conditions apply:

$C(R,Z)=0; R<1; Z=0$, this condition is applied to the electrode surface (2-4 from the geometry in Figure 15). In Comsol this condition is satisfied by applying of Insulation/Symmetry at this boundary.

$\partial C/\partial R=0; R=0; 0<Z<L$, this condition is applied to the boundary 1-2 in Figure 15 (in Comsol it corresponds to Insulation/Symmetry).

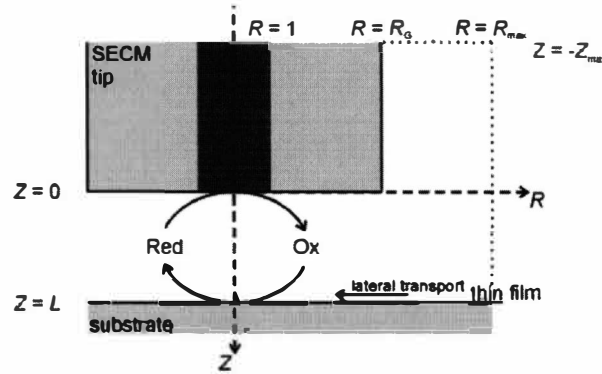


Figure 16 Schematic of the experiment and the definition of the coordinates ².

$C(R,Z)=1; R=R_{max}; -Z_{max}<Z<L$, this condition is applied to the boundary 9-8 in Figure 15 (in Comsol it corresponds to Concentration).

$C(R,Z)=1; R>R_G; Z=-Z_{max}$, this condition is applied to the boundary 7-9 in Figure 15 (in Comsol it corresponds to Concentration).

$\partial C/\partial R=0; R=R_G; -Z_{max}<Z<0$, this condition is applied to the boundary 6-7 in Figure 15 (in Comsol it corresponds to Insulation/Symmetry).

$\partial C/\partial Z = 0; 1 < R < R_G; Z = 0$, this condition is applied to the boundary 4-5-6 in Figure 15 (in Comsol it corresponds to Insulation/Symmetry).

L is normalized tip-substrate distance, $L = d/a$ (d is the physical distance to the electrode, $d = d_0 - d$, a is the electrode radius)

R_G is the ratio between the overall tip radius and the radius of the electrode

$R = r/a$ (r is the radial coordinate, spatial variable)

$Z = z/a$ (z is the axial coordinate, spatial variable)

$C = c/c^b$ (c is the redox couple concentration at a given time, c^b is the bulk concentration of the initially present redox couple)

In the model $Z_{max} = 20$ and $R_{max} = R_G + 20 = 25.4$ were used.

The domain equation 3.7 related to the bulk properties was Fick's⁴³ second law for the axisymmetric diffusion:

$$\frac{\partial C(R, Z, \tau)}{\partial \tau} = D \left[\frac{\partial^2 C(R, Z, \tau)}{\partial R^2} + \frac{1}{R} \frac{\partial C(R, Z, \tau)}{\partial R} + \frac{\partial^2 C(R, Z, \tau)}{\partial Z^2} \right] \quad (3.7)$$

where $\tau = 4Dt/a^2$ (D is diffusion coefficient, t is time) or in more general form:

$$\frac{\partial C}{\partial t} = D \nabla^2 C \quad (3.8)$$

where ∇^2 is Laplacian operator for different geometries.

In Comsol the domain equation looks as is shown in Figure 17. It defines the diffusion problem.

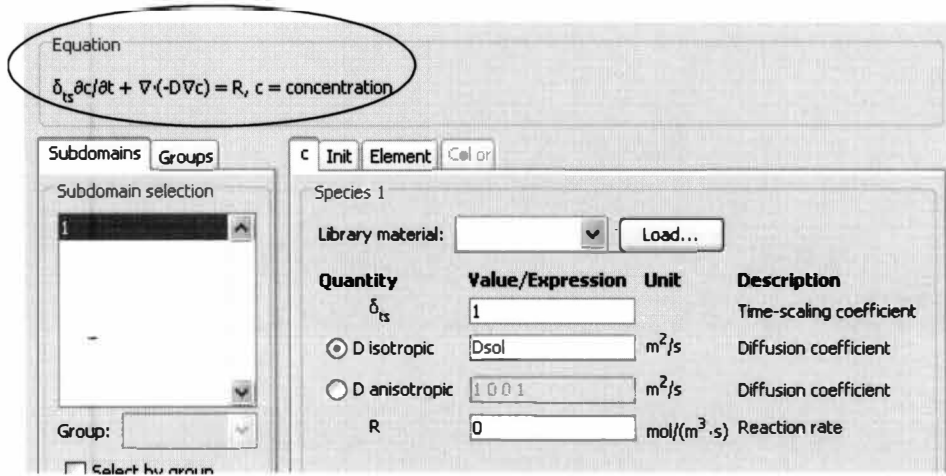
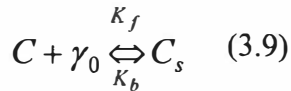


Figure 17 Comsol equation for the diffusion problem.

Under steady-state, the concentration does not change with time so that the first term $\delta_{ts} \partial c / \partial t$ is zero.

The reaction on the surface of the active sites is given as:



where C is the dimensionless bulk concentration, γ_0 ($\gamma_0 = \Gamma / (c^b a)$) is the dimensionless surface concentration of the active sites, C_s is the surface concentration of the reduced species, and K_f and K_b are the corresponding rate constants. It has to be noted that the concentration of the active sites is equal to the difference between the maximum surface concentration of active sites and the number of reacted sites (reduced surface species), $\gamma_0 = \gamma - C_s$.

Equation 3.10 is the boundary condition at the substrate for the electron transfer between the solution redox couple and the nanoparticles film. It shows the material balance for the surface describing surface diffusion and the reaction rate expression for

the formation of reduced species at the nanoparticles film surface.

$$\frac{\partial C_s}{\partial t} + \nabla \cdot (-D_{ss} \nabla C_s) = K_f C(\gamma - C_s) - K_b C_s \quad (3.10)$$

where:

$C_s = \Gamma/\Gamma_{max}$ dimensionless surface concentration (Γ is the surface concentration of reduced surface species, Γ_{max} is the total number of active sites).

$\gamma = \Gamma_{max}/(c^b a)$ dimensionless maximum surface concentration of the active sites available at the nanoparticles film (c^b is the bulk concentration of the redox mediator).

$D_{ss} = D_{surf}/D_{sol}$ dimensionless surface diffusivity (D_{surf} is the surface diffusivity, D_{sol} the diffusion coefficient of the solution redox mediator).

$K_f = k_f \Gamma_{max} a / D_{sol}$ dimensionless rate constant for the forward reaction (k_f is the rate constant for the forward reaction, a is the electrode radius).

$K_b = k_b \Gamma_{max} a / D_{sol}$ dimensionless rate constant for the backward reaction (k_b is the rate constant for the backward reaction).

The initial condition is that the concentration of reduced surface species is zero at the beginning of the process, $C_s = 0$. The equation for the surface reaction expression 3.9 includes the concentration of the bulk species, C , at the position of the nanoparticles film surface. Hence, the equation for the surface reaction was solved in combination with the mass balance in the bulk. The coupling between the mass balance in the bulk and the surface was achieved as a boundary condition in the bulk's mass balance. This condition set the flux of C at the boundary defined between the points 1 and 3 in Figure 15 equal to the rate of the surface reaction expressed by the equation 3.10 above.

The boundary condition given in Quinn's paper², which is related to the lateral charge transport was not included in this simulation. Rather the boundary condition set at

the rest of the substrate (between points 3-8 in Figure 15) was Insulation/Symmetry.

Figure 18 shows the steady-state diffusion at a disk microelectrode in a simulated SECM experiment when the tip is far from the substrate. The concentration profile is shown in a color scale. Immediately at the electrode surface the concentration is zero, because all initially present reduced species are instantly converted to their oxidized form near the SECM tip.

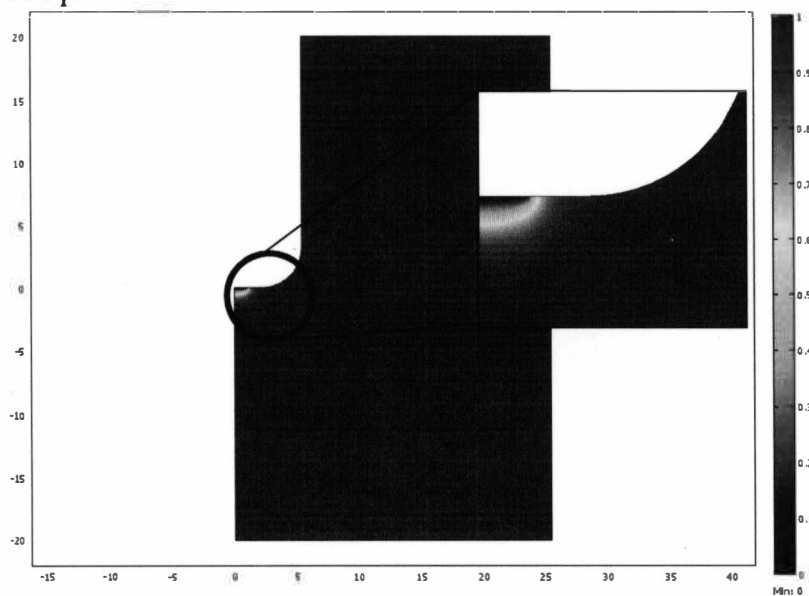


Figure 18 Steady-state concentration profile at the SECM tip.

MathLab connected to Comsol was used to simulate the movement of the SECM tip to the surface by taking the current response at the tip at different positions along the approach (the MathLab program is given in the appendix). The dimensionless tip current was calculated from:

$$Z(\tau) = \frac{i(\tau)}{i_{ss}} = \int_0^1 2\pi R D \left[\frac{\partial f(R, 0, \tau)}{\partial Z} \right]_{Z=0} dR \quad (3.11)$$

$$\text{where } \tilde{f}(R, Z, \tau) = \frac{C(r, z, t)}{c^b}$$

In Comsol, the current was calculated by integration of the boundary representing the electrode surface (2-4 in Figure 15) at a given Z .

Figure 19 displays the simulated approach curve.

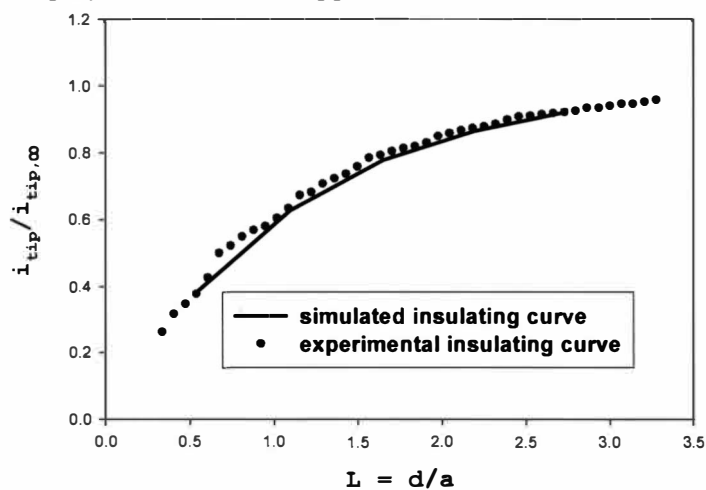


Figure 19 An approach curve (dots) to an $\text{Au}_{38}\text{MPCs}$ film taken with $1000 \mu\text{M}$ FcMeOH in $\text{LiCl}/\text{H}_2\text{O}$ and the corresponding simulated theoretical curve (solid line).

The current decreases with decreasing the tip substrate gap, which is typical for an approach of an insulating substrate. There is a good agreement between the experimental and the simulated theoretical curve.

CHAPTER IV

SECM STUDY OF LIPID MONOLAYERS

Scanning electrochemical microscope (SECM) has been developed as a powerful technique for quantitative investigation of interfacial physicochemical processes. The transport processes at cell membranes are of vital biological importance and a lipid monolayer constitutes a useful model system for investigating electron transfer processes. SECM was successfully applied in the study of molecular, ion, and electron transfer processes at liquid interfaces modified with lipid monolayers⁴⁴⁻⁴⁷. In the current work an electroactive material was added to a lipid monolayer and transferred to a solid substrate to investigate the lateral and long-range electron transport through the lipid monolayer.

Lipids are the main constituents of cell membranes. A typical membrane lipid molecule has a hydrophilic head and hydrophobic tail. The amphiphilic nature of the lipids allows a facile monolayer formation at the air/water interface. The well-defined monolayer can be transferred to a solid substrate for further investigation. Figure 20 shows a scheme of the lipid model system on a glass substrate. Electroactive species (decamethylferrocene, DmFc) are incorporated in the lipid matrix and electron transport processes through the monolayer were investigated using SECM.

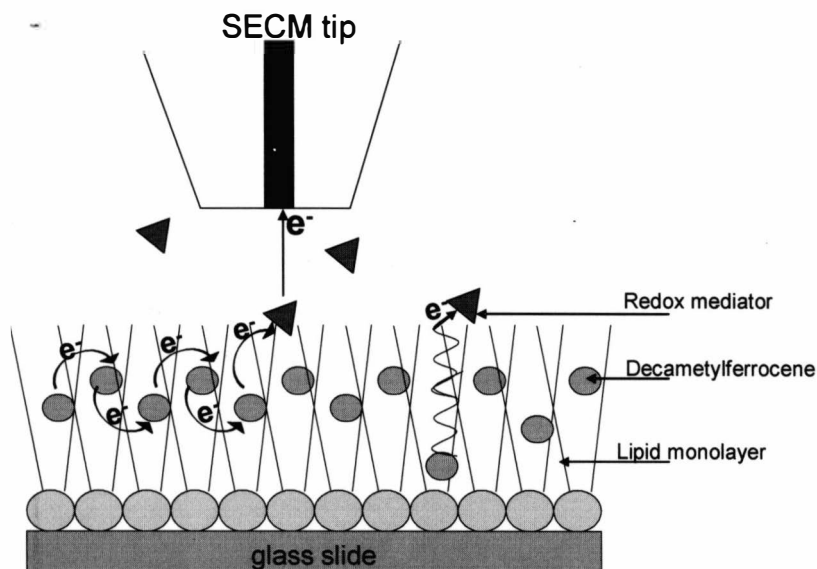


Figure 20 Electron transport pathways in mixed DmFc-lipid monolayer deposited on a glass substrate. Curved arrows show electron “hopping”. Zigzag arrow shows physical diffusion to the surface. Red ellipses are the redox mediator in the bulk solution.

Since the DmFc molecules are free to move in the lipid, the overall electron transport is the summation of the DmFc physical diffusion to the outer boundary of the monolayer (where the SECM tip is located), and the electron “hopping” between DmFc molecules in close proximity. The apparent diffusion of electrons in a film can be described by the Dahms-Ruff equation⁴³:

$$D_{app} = D_{phys} + D_E \quad (4.1)$$

The apparent diffusion coefficient observed for DmFc, D_{app} , is composed of contributions from its physical movement, governed by its actual mass-transfer diffusion coefficient, D_{phys} , and the electron diffusion coefficient, D_E .

The initial work in this study was to find a suitable lipid monolayer system. The monolayer transfer to a solid substrate was confirmed by adding a fluorescence probe. A

redox probe was incorporated into the lipid monolayer, in order to generate an electron flow for the SECM measurement. The contact angle measurements, however, revealed that the quality of the transferred monolayer was a serious concern. Therefore the resistant glass substrate was changed to a conductive indium tin oxide (ITO), in order to perform electrochemical measurement of the DmFc in the lipid matrix. The overall result showed that the system quality needs to be improved for using as a substrate with the SECM.

4.1 Lipid monolayers of different chain-lengths at the air/water interface

The surface-area per molecule (π -A) isotherms of various lipid monolayers on pure water are shown in Figure 21: DDPC (10:0), DLPC (12:0), DMPC (14:0), DPPC (16:0), DSPC (18:0), and DAPC (20:0). The first number in the parenthesis represents the number of the tail carbons and the second number represents the number of the double bounds in the tail. The insets in Figure 21 show the lipid structures. Every isotherm, also called pressure-area (π -A) isotherm is unique for a given lipid and it can be used to characterize a particular monolayer system⁴⁸.

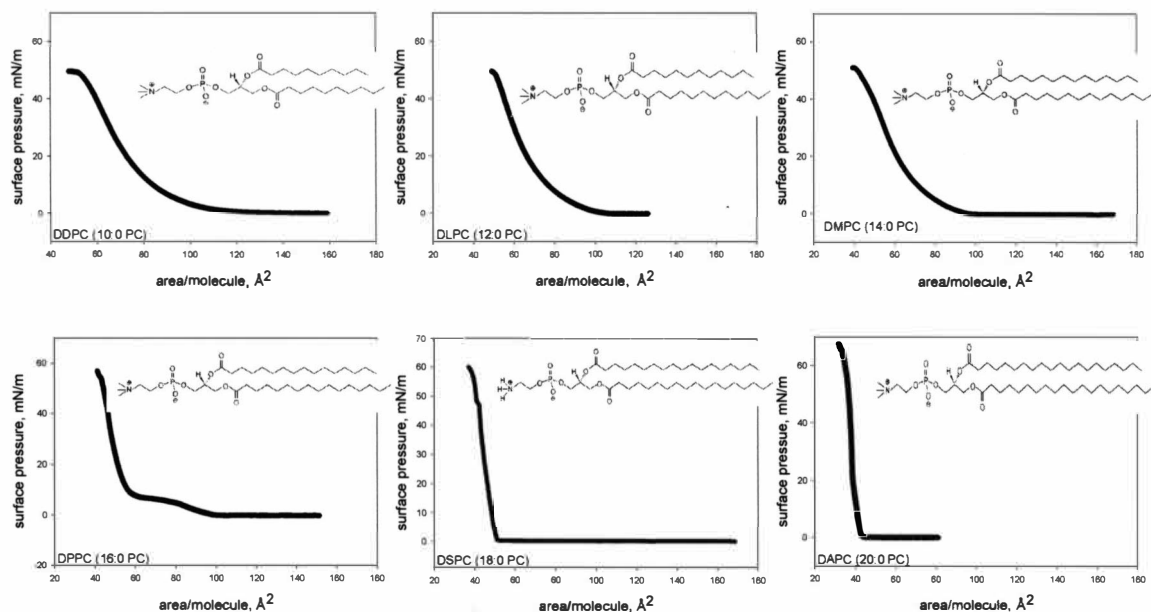


Figure 21 Surface pressure(π)-area(A) isotherms of saturated lipids with chain lengths of C10, C12, C14, C16, C18, and C20.

The lipid is in its most disordered state at the isotherm beginning, where the surface pressure is 0 mN/m. By decreasing the area per molecule, the surface pressure increases and the lipid monolayer undergoes phase transitions of ordering from gas-liquid to liquid, to liquid-solid, and to solid state. If the monolayer is further compressed after reaching the solid state, the monolayer collapses into three-dimensional structures.

Table 1 lists collapse pressures, phase transition temperatures, and area per molecule. The area occupied by one molecule was taken by extrapolation of the steepest region from the isotherm plot. Phase transition temperatures are from the Avanti website⁴⁹, from which all lipids were purchased. The collapse surface pressure corresponds to the breaking point where the full monolayer package is attained and applying additional pressure leads to destroying the monolayer structure (collapse).

Beyond this point the collapse of the monolayer is seen as a rapid decrease or as a horizontal break.

Lipid	Collapse surface pressure, [mN/m]	Phase transition temperature, [° C]	Area, Å ² /molecule
DDPC (10:0)	49	-33	88.8± 7.4
DLPC (12:0)	50	-1	82.6± 3.1
DMPC (14:0)	51	23	73.7± 3.4
DPPC (16:0)	55	41	60.9± 0.4
DSPC (18:0)	60	55	53.0
DAPC (20:0)	65	66	50.2

Table 1 Collapse surface pressure, phase transition temperature, and the area occupied by one molecule for saturated lipids with chain lengths of C10, C12, C14, C16, C18, and C20. DDPC and DLPC are in fluid phase at room temperature, DMPC is in phase transition, and DPPC, DSPC, and DAPC are in gel phase.

As the hydrocarbon length increases, van der Waals interactions become stronger^{48, 50} and pull the lipid molecules closer together requiring more energy to disrupt the ordered packing. Thus, the collapse pressure and phase transition temperature increase, but the area per molecule decreases. The area is determined by the size of head groups also, smaller head groups allow shorter distance between the chains and better packing under applied pressure. Also these factors are closely related to the phase transition temperature, which varies with lipids.

The stability of a monolayer was examined by performing of repeated expansion and compression cycles of the monolayer. Figure 22 and Figure 23 show cycling isotherms of saturated and unsaturated lipids respectively.

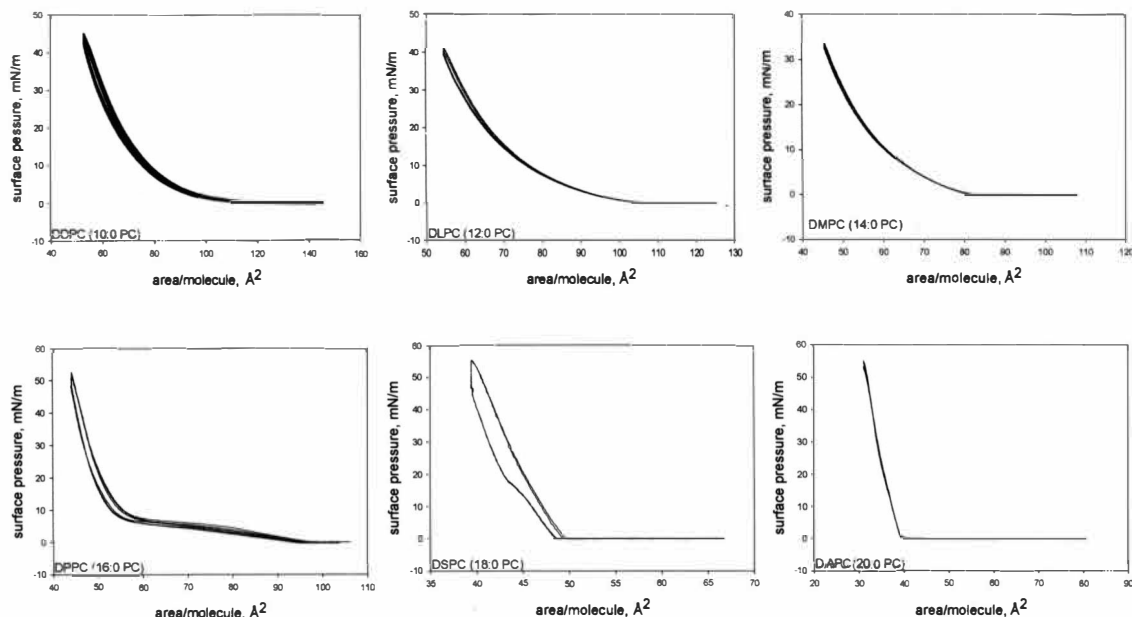


Figure 22 Compression-expansion cycling of 6 saturated lipids with different chain lengths: DDPC (10:0), DLPC (12:0), DMPC (14:0), DPPC (16:0), DSPC (18:0), and DAPC (20:0). In the parenthesis are: the first number representing the number of the tail carbon atoms and the second number representing the number of the double bonds along the tail.

Although there is hysteresis between the compression and expansion cycles, the isotherms of the saturated lipids were reproducible in contrast to the unsaturated lipids examined. Figure 23 shows that the surface pressure at a given area attained decreases with cycling, indicating less material on the surface supporting high surface pressure. The lack of reproducibility indicates that aggregation, crystallization, or collapse may occur on the unsaturated lipid monolayers⁵¹.

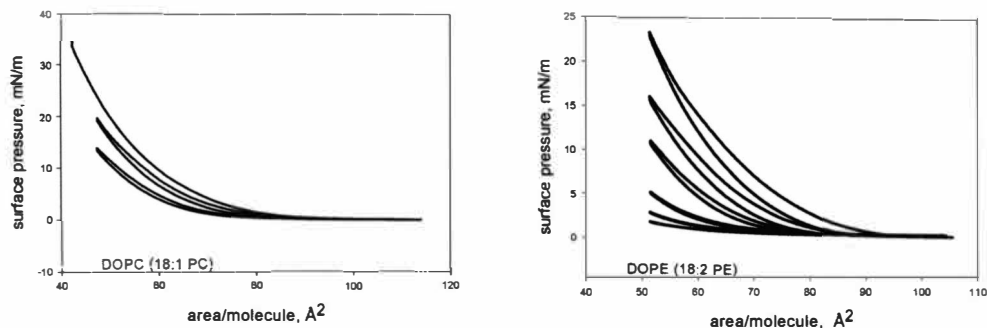


Figure 23 Compression-expansion cycling of unsaturated lipids. DOPC (18:1) and DOPE (18:2) isotherm cycles.

The current study is based only on lipids with saturated hydrocarbon chains, because of their high monolayer stability. The monolayer area of used saturated lipids was stable over time at a constant pressure and it underwent collapse at higher pressure.

4.2 Langmuir-Blodgett transfer of lipids to a solid substrate

Langmuir-Blodgett (LB) technique was employed for all monolayer transfers. Since phospholipids are nonfluorescent, spectroscopy with monolayers of them is possible only if suitable dye is incorporated. In this study NBD-PE was used as a dye. The extrapolation of the steepest region of the dye isotherm (Figure 24) gave its molecular size of 74.1 \AA^2 . From Table 1, the lipid with the closest molecular size to this value is DMPC. Hence, for further investigation the system of DMPC and NBD-PE was chosen in order to prevent a distortion of the lipid monolayer by the dye addition.

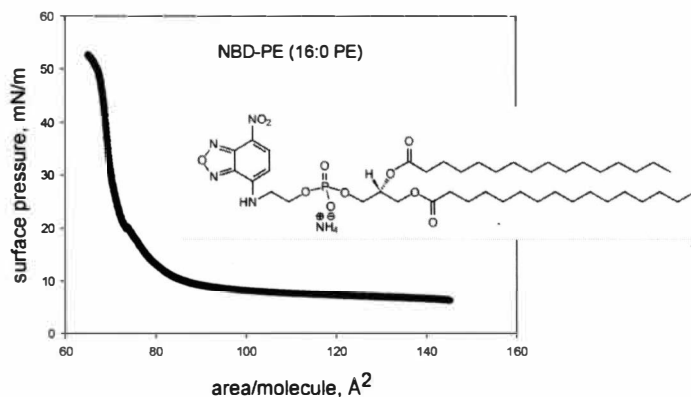


Figure 24 Surface pressure(π)-area(A) isotherm of the dye molecule NBD-PE.

As alternative lipids DPPE (16:0) and DMPE (14:0) were tested for their molecular size, area per molecule at the solid state. NBD-PE (16:0) has the same structure of the head group (phosphoethanolamine) and the same chain length (sixteen carbons) as DPPE. DMPC has the same chain length of fourteen carbons as DMPE. Figure 25 displays the isotherms of DPPE and DMPE.

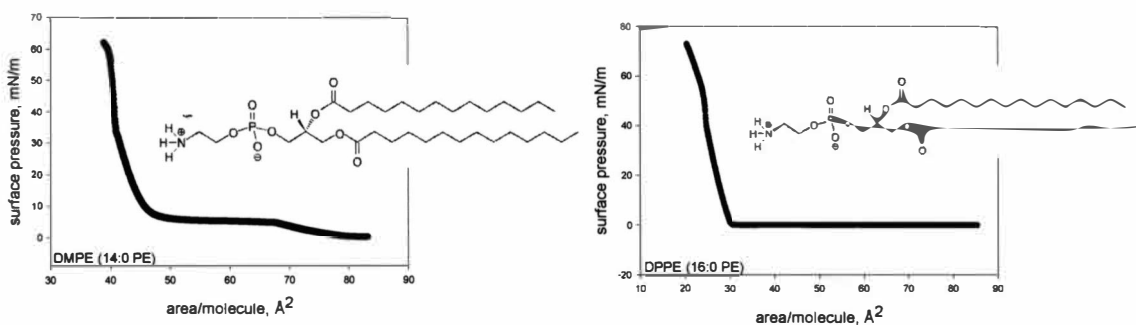


Figure 25 Surface pressure(π)-area(A) isotherms of DMPE (14:0) with area/molecule 42.5 \AA^2 and DPPE (16:0) with area/molecule 29.6 \AA^2 .

It was found that DPPE, DMPE and NBD-PE have different strengths of intermolecular interactions as reflected by their significantly different areas per molecule.

Therefore DPPE and DMPE were not used as substituents for the DMPC lipid.

PC (phosphocoline) lipids were deposited onto a hydrophilic glass substrate or hydrophobic one ($((\text{CH}_3)_2\text{Cl}_2\text{Si})$ treated glass slip). Figure 26 shows the results from LB deposition of DLPC (12:0) at four different surface pressures on a hydrophobic substrate. The starting point was dipping of the substrate down from air in water when the first layer was formed. It was followed by pulling up the substrate until the whole substrate was in air (second layer formation).

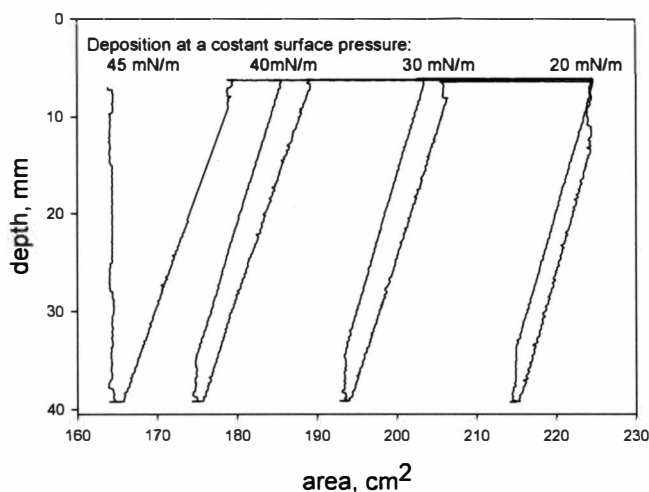


Figure 26 LB deposition of DLPC (12:0) on a hydrophobic substrate ($((\text{CH}_3)_2\text{Cl}_2\text{Si})$ treated glass slip) at different surface pressures: 20, 30, 40, 45 mN/m. Successful transfer achieved only at 45 mN/m.

The plot in Figure 26 is the area between both barriers versus the depth of the immersed substrate. At constant pressure 20 mN/m the area did not change during immersing and withdrawing of the hydrophobic substrate (it starts and ends at the same point 225 cm²). There was negligible deposition on the substrate at 30 and 40 mN/m pressures. A successful transferring of the DLPC was observed at 45 mN/m. The change (initial and final point) of the area (15 cm²) between the barriers corresponded to the

transferred monolayer portion.

Figure 27 displays a deposition of DMPC (14:0) on a hydrophilic substrate. In this case the deposition started by pulling up of the substrate from a given depth and resulted in transferring a single layer. The surface pressure during deposition was kept at 25 mN/m and the transferring efficiency monitored by the area decreased during the deposition.

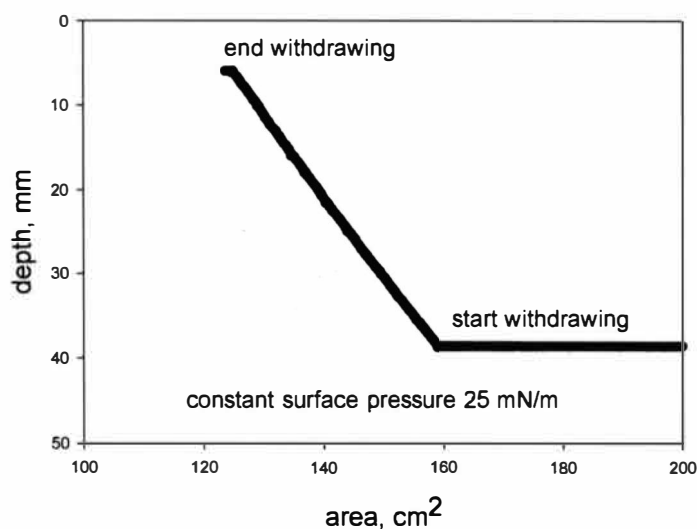


Figure 27 Deposition of DMPC (14:0) on a hydrophilic substrate at surface pressure of 25 mN/m.

The results indicated that the lipid deposition can be achieved at high and low surface pressures (25 mN/m - 45 mN /m), in the case of a hydrophilic glass substrate, but only at high pressures (~45 mN/m) in the case of a hydrophobic substrate. This was related to the charge of the PC head groups (positive at amino group and negative at phosphate group at natural pH); the formation of electrostatic forces between the hydrophilic glass surface and the lipid heads⁵². In contrast, the deposition on a hydrophobic substrate occurs as a result of hydrophobic interactions between the

hydrocarbon tails of the lipid and the hydrophobic substrate (silanized glass slip), which requires close proximity of the lipid molecules achieved only at high pressures.

Next step was examining the isotherm of the dye-lipid monolayer. The dye was added to the lipid dissolved in chloroform with concentration of 1 mol % NBD-PE to DMPC. The observed isotherm differed slightly from that of a pure DMPC (Figure 28). This indicates that the addition of the dye did not perturb the lipid layer significantly.

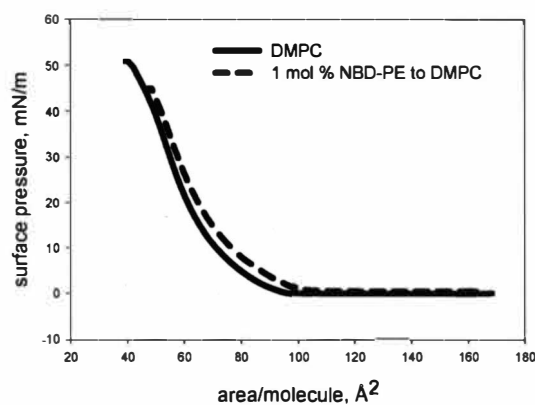


Figure 28 Comparison of pressure(π)-area(A) isotherms of pure DMPC and 1 mol% NBD-PE/DMPC.

By combining both DMPC (14:0) and NBD-PE (16:0) into one system, it was possible to detect absorption of the dye in the mixed monolayer after its deposition on a glass slip. NBD-PE excitation occurs at 460 nm and the maximum emission occurs at 534 nm which is shown in Figure 29.

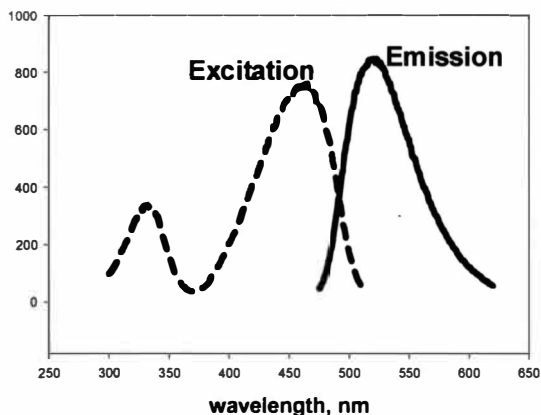


Figure 29 Fluorescence spectra of NBD-PE in chloroform solution.

Figure 30(a) demonstrates the UV-VIS spectrum of 1 mol % NBD-PE in DMPC in chloroform solution. Before transfer, the same solution was spread for a monolayer formation in the trough. Figure 30(b) displays a spectrum taken from a deposited pure NBD-PE bilayer, and Figure 30(c) shows that despite the small amount of NBD-PE (1 mol %), it is possible to observe its absorption signature due to its relatively high molar absorptivity ($\sim 20,000 \text{ cm}^{-1}\text{M}^{-1}$)⁵³. The absorption peak from the supported NBD-PE was shifted by 14 nm with respect to that from the solution (460 nm). It may be due to the different environment and the immobilization on the substrate.

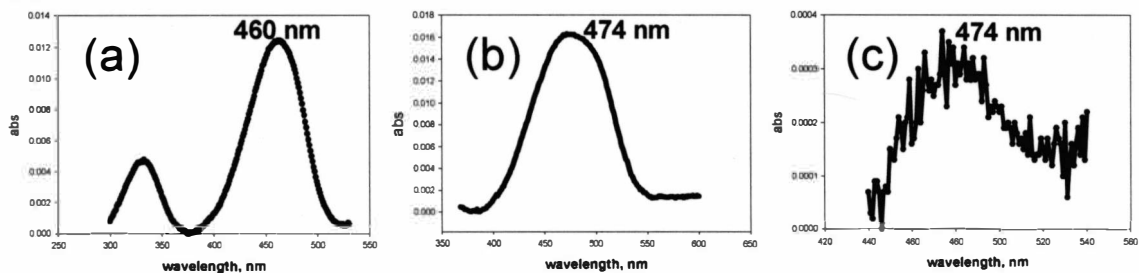


Figure 30 UV-Vis absorption spectra of (a) 1 mol% NBD-PE/DMPC in chloroform, (b) NBD-PE monolayer on a silanized glass substrate, and (c) 1 mol% NBD-PE/DMPC monolayer on a silanized glass substrate.

Further investigation of the dye-lipid system was performed by observing the supported monolayer fluorescence. The frame (a) in Figure 31 shows relatively even fluorescence from the surface of 1 mol % NBD-PE to DMPC contrary to the non-glowing frame (b) where the excitation light beam was off. Frame (c) was taken at the edge of the substrate where the light part is the glowing monolayer and the dark part is the area with no monolayer.

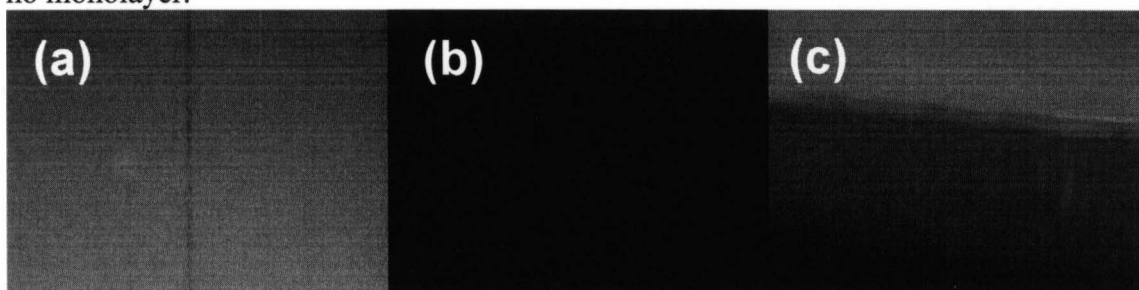


Figure 31 Fluorescence of 1 mol% NBD-PE/DMPC monolayer taken with Nikon epi-fluorescence microscope.

The ability to photobleach a spot in the deposited monolayer also supported the successful transfer and showed that the monolayer was on the substrate (Figure 32). In spite of the large bleached spot (500 μm) and the DMPC crystalline phase at room temperature, the recovery occurred after 45.5 hours.

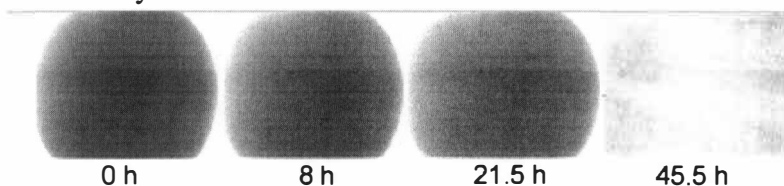


Figure 32 Fluorescence recovery after photobleaching (FRAP) of 1 mol% NBD-PE/DMPC monolayer.

Overall, the results from the UV-VIS indicated the dye presence as a consequence

of its successful transfer. The fluorescence measurements showed that on a micrometer scale the lipid monolayer is uniform.

4.3 Redox probe incorporated lipids for SECM measurements: DmFc-DMPC

For SECM measurements, the substrate needs to be in contact with the electrolyte solution. The electrolyte solution consists of supporting (base) electrolyte and electroactive species (redox mediator). To find the supporting electrolyte limitation (working range of the potential) two base electrolytes NaClO_4 and KCl were examined.

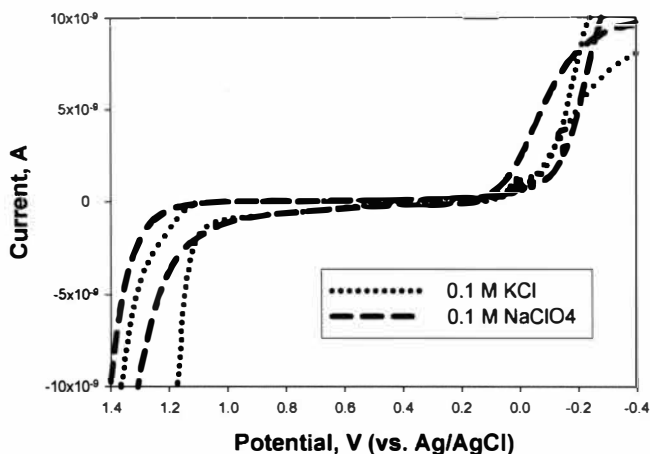


Figure 33 Cyclic voltammograms of only supporting (base) electrolytes: 0.1 M KCl and 0.1 M NaClO_4 at a Pt electrode.

The potential limits with a Pt working electrode were similar in both cases (Figure 33). Mainly NaClO_4 was used because of its suitability to all examined aqueous redox mediators. For example, $\text{Ru}(\text{bpy})_3^{2+}$ was used with NaClO_4 , because it reacts with KCl to form $\text{Ru}(\text{bpy})_3\text{Cl}_2$ precipitates in aqueous solution.

The next step was to screen a few redox mediators with different formal potentials - $\text{K}_4\text{Ru}^{\text{II}}(\text{CN})_6$, $\text{Ru}^{\text{II}}(\text{bpy})_3\text{Cl}_2$, $\text{K}_4\text{Mo}^{\text{IV}}(\text{CN})_8$, and FcMeOH . The cyclic voltammograms

shown in Figure 34 were used to extract formal potentials of the redox couples and to calculate their diffusion coefficients (equation 3.2) given in Table 2.

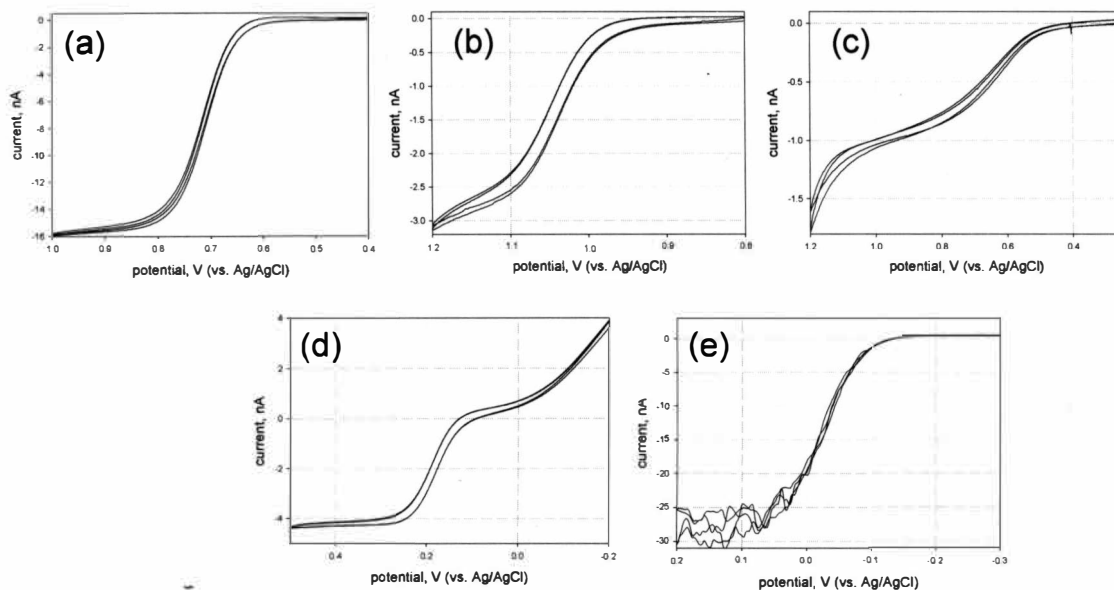


Figure 34 Cyclic voltammograms (CVs) of five redox couples: (a) 5 mM $\text{Ru(II)(CN)}_6\text{K}_4$ /0.1 M NaClO_4 in H_2O , (b) 1 mM $\text{Ru(II)(bpy)}_3\text{Cl}_2$ /0.1 M KNO_3 in H_2O , (c) 0.36 mM $\text{Mo(IV)(CN)}_8\text{K}_4$ /0.1 M NaClO_4 in H_2O , (d) 1 mM FcMeOH /0.1 M NaClO_4 in H_2O , and (e) 5 mM DmFc (decamethylferrocene)/0.1 M TBA.ClO_4 in DCE (dichloroethane). All CVs were taken at scan rate of 10 mV/s.

The redox mediator's diffusion coefficients (Table 2) were calculated by applying equation 3.2 to the steady-state current (limiting current) at a disk microelectrode.

Redox species	Formal Potential E^o (V) vs Ag/AgCl	Diffusion coefficient, D (cm ² /s)
$\text{Ru}(\text{CN})_6^{4-}/\text{Ru}(\text{CN})_6^{3-}$	0.75	5.0×10^{-6} in 0.1 M $\text{NaClO}_4/\text{H}_2\text{O}$
$\text{Ru}(\text{bpy})_3^{2+}/\text{Ru}(\text{bpy})_3^{3+}$	1.04	4.7×10^{-6} in 0.1 M $\text{KNO}_3/\text{H}_2\text{O}$
$\text{Mo}(\text{CN})_8^{4-}/\text{Mo}(\text{CN})_8^{3-}$	0.62	3.7×10^{-6} in 0.1 M $\text{NaClO}_4/\text{H}_2\text{O}$
FcMeOH	0.18	6.9×10^{-6} in 0.1 M $\text{NaClO}_4/\text{H}_2\text{O}$
DmFc	0.025	0.95×10^{-6} in 0.1 M $\text{Bu}_4\text{NClO}_4/\text{DCE}$

Table 2 Formal potentials and diffusion coefficients of five redox couples.

The electroactive species incorporated in the lipid layer was decamethylferrocene (DmFc), which structure is shown in Figure 35.

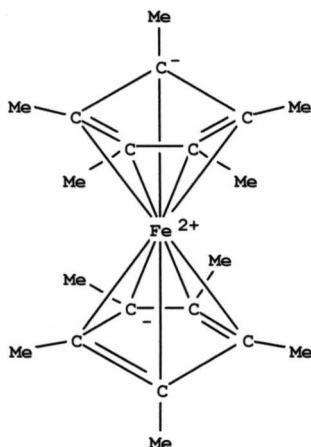


Figure 35 Decamethylferrocene (DmFc) structure. Neutral molecule with an iron atom in 2+ oxidation state.

Decamethylferrocene (DmFc) diffusion coefficient in the lipid environment is unknown, but it can be estimated to be in order of 10^{-9} cm²/s or higher, comparing with diffusion coefficients $1-4 \cdot 10^{-9}$ cm²/s of cell membrane proteins⁵⁴ that are larger than

DmFc.

The isotherm of DmFc-DMPC monolayer is shown in Figure 36.

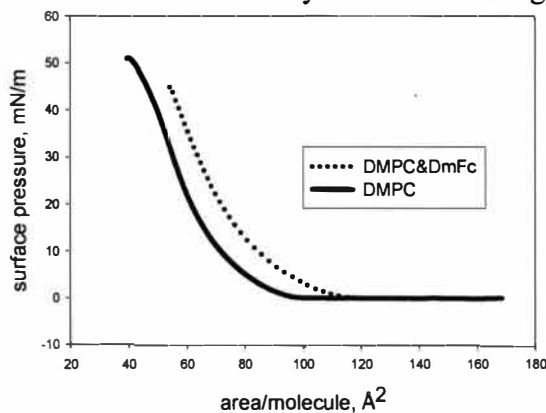


Figure 36 Comparison of pressure(π)-area(A) isotherms of pure DMPC and 20 v/v % DmFc/DMPC monolayer.

There is a small difference between the isotherms of pure DMPC and DmFc-DMPC. Hence, addition of the redox probe (DmFc) did not cause significant distortion of the lipid matrix. DmFc was calculated to be 20 v/v % of the lipid, assuming that it is a sphere with hydrodynamic radius of 0.38 nm⁵⁵. It was necessary to add this high amount of DmFc, in order to reach the percolation threshold of ~ 0.25 metal volume fraction⁵⁶. At the percolation threshold, at least a single conduction pathway through the system is established, which is a necessary condition for observing electron transport with DmFc.

The lipid volume was calculated based on its occupied area in the Langmuir-Blodgett trough and a height of 15.6 Å taken from the AFM image in Figure 37.

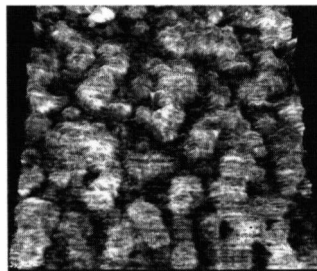


Figure 37 AFM image of DMPC (14:0) lipid.

The SECM experiment of the DmFc-DMPC system was performed with an examination of $\text{Mo(CN)}_8^{4-/3-}$ as an aqueous redox mediator (Figure 38), in order to detect the electron transport in the monolayer. When the SECM tip is within a few tip radii close to a substrate, a perturbation of the steady state current occurs. Since the substrate has a lipid layer with DmFc inside, the electron transport in the monolayer would result in a bimolecular reaction at the SECM tip between oxidized species (Mo(CN)_8^{3-} generated at the tip) from the aqueous solution, and DmFc species from the monolayer:



$\text{Mo(CN)}_8^{4-/3-}$ is a suitable redox mediator for this experiment, because the electrochemical potential of DmFc is lower (0.025 V, Table 2) than the one of octacyanomolybdate (0.62 V, Table 2) and the reaction 4.2 above is thermodynamically favorable.

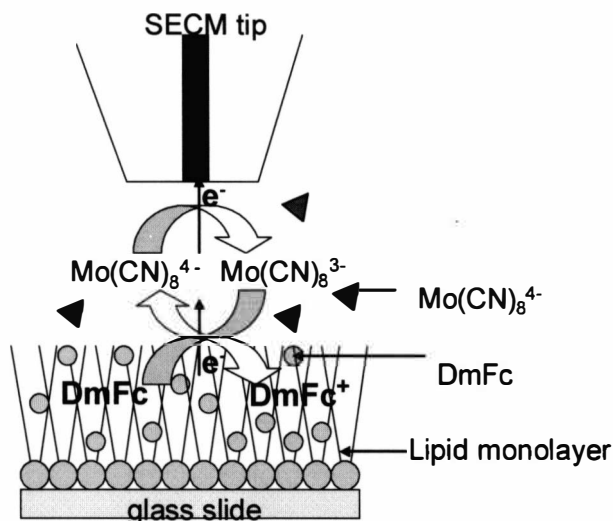


Figure 38 Scheme of SECM experiment with mixed DmFc-lipid monolayer.

The electron transport (ET) properties of mixed lipid-DmFc monolayer were examined by SECM. The tip current (i_{tip}) collected during SECM approach experiments is a summation of serial reactions such as ET between $\text{Mo(CN)}_8^{4-/3-}$ molecules in the aqueous phase, ET between DmFc molecules in the lipid, and ET between DmFc and Mo(CN)_8^{3-} . The slowest process determines the rate limiting step and resolves the tip current response. The ET of DmFc- Mo(CN)_8^{3-} and $\text{Mo(CN)}_8^{4-/3-}$ itself is fast, therefore the tip current is only controlled by the rate of electron transport in the lipid monolayer.

The result from the SECM experiment is displayed in Figure 39. The redox mediator concentrations were either 1 mM or 0.1 mM.

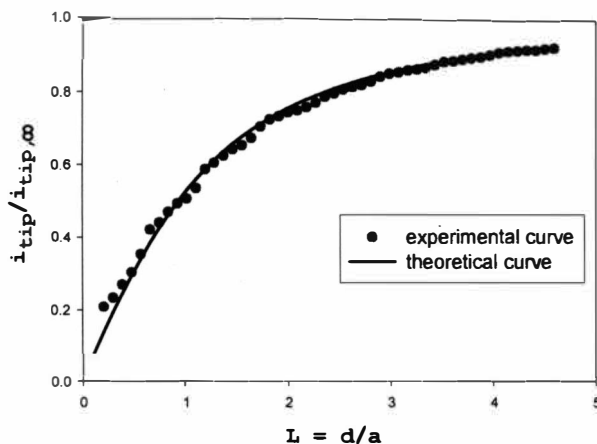


Figure 39 Experimental approach curve (dots) to DmFc-DMPC monolayer. It fits well to the theoretical pure negative feedback (solid line).

The approach curves always demonstrated negative feedback as the example shown in Figure 39. It means that there is no ET between DmFc from the monolayer and $\text{Mo}(\text{CN})_8^{3-}$ from the solution. The observed negative feedback was due to hindered diffusion to the SECM tip. For observation of the lateral electron transport in a monolayer of gold nanoparticles, a sufficient decrease of the redox mediator concentration has been required ($<10 \mu\text{M}$)^{2, 57}. In the case here, the reducing of the redox mediator concentration probably was not adequate.

4.4 Contact angle measurements

Contact angle measurements were carried out on the supported monolayer samples. A cover glass slip used as a substrate had a contact angle close to 0° . An indium tin oxide (ITO) was used as a conductive substrate, which is also a hydrophilic surface. Its static contact angle was higher $24.7^\circ \pm 1.1^\circ$ (Table 3). The values reported in Table 3 are averages of 3 measurements made on different areas of the sample surface at 20°C ,

below the lipid (DMPC) phase transition temperature ($T_m = 23^\circ$)⁴⁹. The same temperature was maintained when the monolayer transfer was performed to keep optimum deposition conditions.

After a monolayer deposition the hydrophilic lipid heads were stacked on the hydrophilic substrate and the hydrophobic lipid tails were exposed to the air. Hence, the expected contact angle of a close packed lipid film was greater than 90° . In the literature for a $-\text{CH}_3$ terminated surface prepared by self-assembly monolayer (SAM) of alkanethiol, the advancing and receding contact angles are about 110° and 92° , respectively⁵⁸.

The contact angles in this study were much smaller. There are two possible reasons. First, the monolayer was not fully covered but contains exposed glass surface. Second, the molecules were not oriented completely with hydrophobic tails faced outward. Both reasons are possible, because in the Langmuir-Blodgett films under investigation here the interaction between deposited molecules and substrate is physical adhesion, and its strength is less than 10 kcal/mol ⁵⁹. Other authors have faced same type of problems. Lee and coworkers⁵¹ have found that advancing and receding contact angles of a deposited DMPC monolayer are 72.2° and 24.8° , respectively. Reinhardt-Schlegel et. al.⁶⁰ have reported microporous structures of DMPC monolayer containing lipid free regions by using a transmission electronic microscope (TEM).

substrate	GLASS		ITO		
system	DMPC	DMPC&DmFc	DMPC	DMPC&DmFc	bare ITO
contact angle, deg	61.0 ± 2.0	55.6 ± 0.8	49.3 ± 1.23	60.0 ± 0.7	24.7 ± 1.1

Table 3 Static contact angles of a water drop on different substrates.

In addition, to find the stability of a mixed DmFc-lipid layer under a water drop, a static contact angle was monitored as a function of time. When a water drop was left on the surface, the contact angles in both cases (glass substrate and ITO) decreased and leveled off at $\sim 52^\circ$ (Figure 40). According to Seitz⁶¹ initial drop of less than 10° is typical for a stable monolayer.

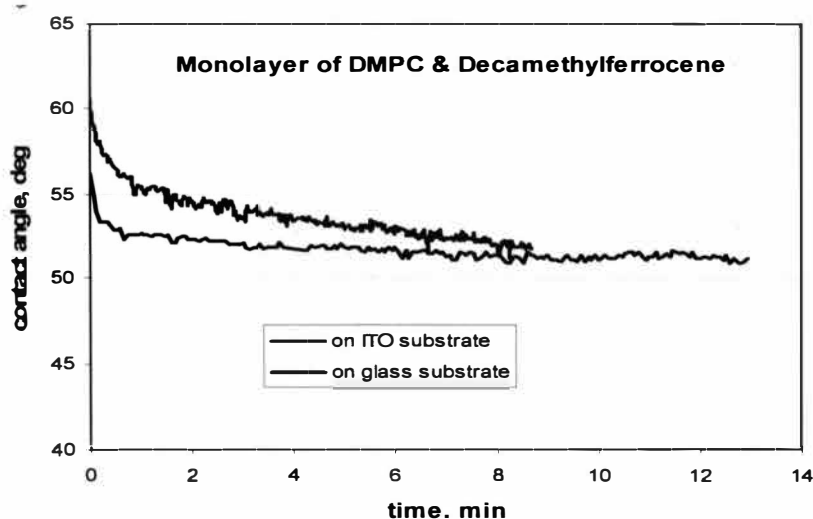


Figure 40 Stability of contact angles on glass and ITO substrates. The glass substrate and ITO covered with 20 v/v % DmFc/DMPC monolayer.

In conclusion, contact angle measurements suggested that the mixed DmFc-lipid layer even though containing voids was stable and could be used for further investigation.

4.5 ITO electrochemistry

In order to perform electrochemical measurements of the decamethylferrocene (DmFc) incorporated in the lipid matrix, a conductive indium tin oxide (ITO) substrate was used instead of the glass substrate. As mentioned earlier, the Langmuir-Blodgett

technique was used for transfer of a plain lipid or a mixed DmFc-lipid monolayer. The prepared ITO in this manner is called “modified electrode” and it was used as a working macroelectrode. The two other electrodes (reference Ag/AgCl and counter Pt wire) were immersed in an electrolyte drop containing only base electrolyte on top of the modified ITO.

The potential technique used for changing the applied potential on the ITO was cyclic voltammetry. Since the decamethylferrocene formal potential is 0.025 V (versus Ag/AgCl, see Table 3 above) the potential at the ITO was scanned in the range from -0.35 to 0.4 V. The resulting cyclic voltammograms of the bare ITO and modified with a mixed DmFc-lipid are shown in Figure 41. There is a definite difference between the system with and without a monolayer. The peaks that showed up at about 0.15 and -0.05 V (solid line) were caused by DmFc oxidation-reduction. The presence of electroactive species in the lipid layer was confirmed.

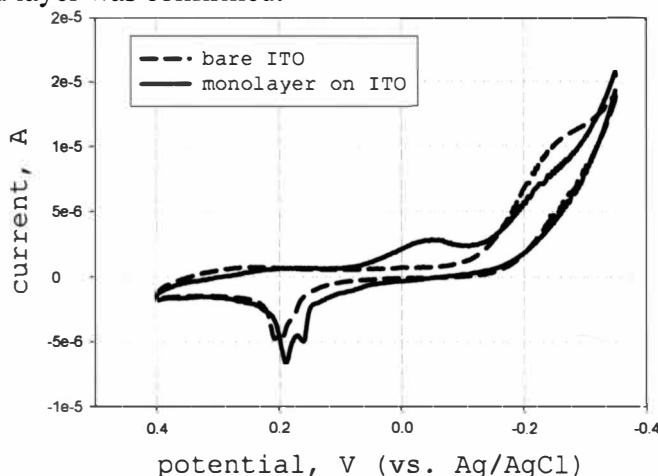


Figure 41 Cyclic voltammograms at a bare ITO and at a modified ITO with a mixed DmFc-lipid monolayer. Electrolyte solution 0.1 M NaClO₄. Scan rate 0.01 V/s. The ITO was used as a macro-working electrode

To find out the electron transport through the monolayer alone, the DmFc was removed from the system. A redox mediator, $\text{Mo(CN)}_8^{4-}/\text{Mo(CN)}_8^{3-}$, was added in the electrolyte drop instead. The experimental set-up is shown in Figure 42. If the plain lipid monolayer is uniform (no defects) and the interaction between the individual molecules is strong enough, the molybdenum ion would not be able to penetrate and reach the ITO electrode surface. The current response at the ITO electrode would be caused only by long-range electron transport through the monolayer and not by physical diffusion.

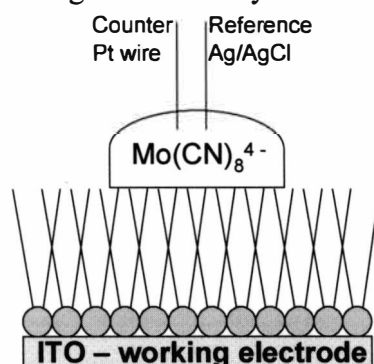


Figure 42 Experimental design of a lipid monolayer modified ITO electrode. An electrolyte drop is placed on top of the monolayer, where the reference and the counter electrodes are immersed.

The voltammogram from the actual experiment is shown in Figure 43. Opposite to the expectations, the current caused by molybdenum oxidation on a modified ITO had the same magnitude as the current caused by molybdenum oxidation on a bare ITO ($\sim 25 \mu\text{A}$).

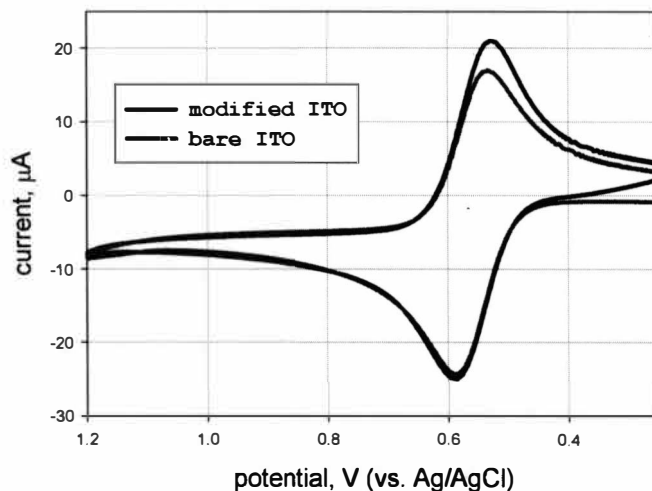


Figure 43 Cyclic voltammogram of $\text{Mo}(\text{CN})_8^{4-}/\text{Mo}(\text{CN})_8^{3-}$ in $\text{NaClO}_4/\text{H}_2\text{O}$ at a bare and a lipid monolayer modified ITO.

Clearly, in this experiment the electroactive species (Mo^{4+}) from the electrolyte drop can communicate freely with the ITO electrode in the presence of the lipid monolayer. This result questioned the monolayer quality and suggested the presence of defects in the monolayer.

The lipid monolayer system with freely diffusing DmFc is not trivial. The contact angle measurements and ITO experiments questioned the quality of the monolayer. Therefore for further investigation of the long-range electron transport through hydrocarbon chains, a better defined system constructed of gold nanoparticles was explored.

CHAPTER V

SECM STUDY OF AUMPCS FILMS

Scanning Electrochemical Microscope (SECM) is an advanced electroanalytical technique for measuring of electron transport in a variety of systems. Previously, this technique has been used to probe lateral charge hopping in redox active monolayers², the insulator-metal transition in a silver nanoparticles monolayer⁶², lateral conductivity in multilayer polymer/gold nanoparticles films⁶³, and monolayer conductivity of gold nanoparticles upon its mechanical compression³. Here the SECM was used to probe size-dependence conductivity in drop cast films of alkanethiolate monolayer protected gold clusters (AuMPCs). These gold nanoparticles bridging small molecules and bulk materials are of intense interest driven by fundamental questions and possibilities to use in nanoscale technology. In addition to their small dimension, the great importance of MPCs is that they are stable as dry chemicals, owing to the protecting monolayer. MPCs resist aggregation of the metal cores in solid state and can be repeatedly isolated and redissolved.

Compared with conventional electroanalytical methods to study conductivity of nanoparticles assemblies, the advantages of using of SECM are that it is noninvasive, highly localized, and does not require the film to be externally biased².

This work describes SECM measurements of four AuMPC samples differing in the gold core size (Figure 44). By varying the core size from 1.1 to ~2.7 nm in diameter and keeping the same thiol chain length, the interparticle separation was decreased in order to observe size-dependant conductivity. In Figure 44 are listed the normalized interparticle distances $d/2a$, where d is the center-to-center distance between adjacent nanoparticles and a is the core radius. For $d/2a$ values > 1.3 , a classical coupling model

has been suggested to account for the experimental observations and for $1.3 > d/2a > 1.2$, a quantum coupling model has been employed⁶⁴.

The interparticle separations ($d/2a$) of the examined samples here (Figure 44) were 1.8, 1.6 and 1.3 and in the case of suitably monodisperse nanoparticles, should be observed a conductivity increasing with the separation decreasing.

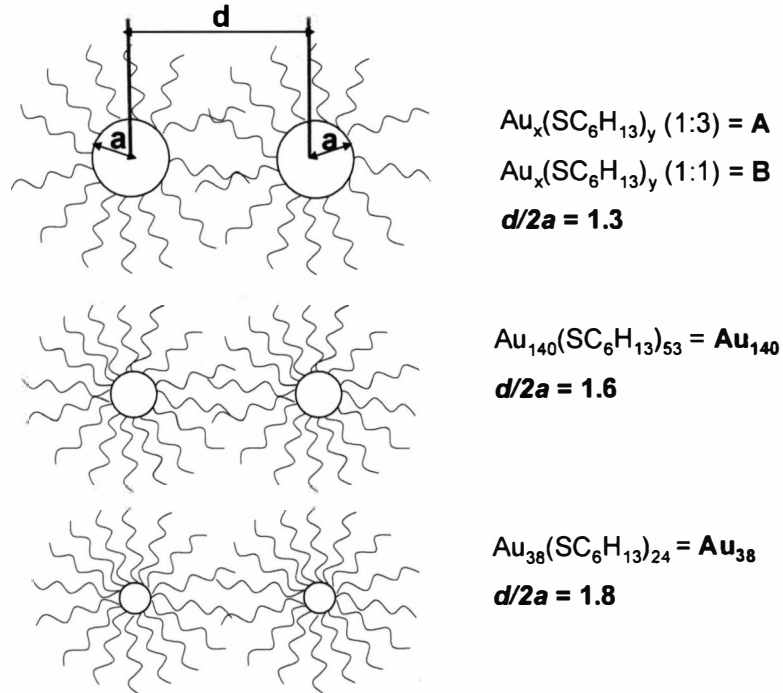


Figure 44 Schematic of the studied gold hexalkanethiolate monolayer protected clusters. The normalized interparticle separation $d/2a$ was same for the first two samples A and B, which have on the same average core size, but different core size dispersity. With decreasing the core size to Au_{140} and Au_{38} MPCs the $d/2a$ value increases.

It has been suggested that the electron transport in solid-state, mixed-valent MPCs occurs by bimolecular electron self-exchange (“hopping”) mechanism⁶⁵. Figure 45 illustrates the diffusion-like electron transport in multilayer films, which involves

electrolysis of a solution redox mediator at a microelectrode (SECM tip), and monitoring the resulting tip current as a function of the tip-film distance. The local depletion of the redox mediator at the film surface sets up an electrochemical potential gradient in the film that causes electron transport to take place. The charge injection (electron supply) in the film was proposed to come from the same redox mediator outside the tip-substrate gap³. Since the films were cast on an inert glass substrate, the measured current was due solely to outside charge injection and electron hopping in the film.

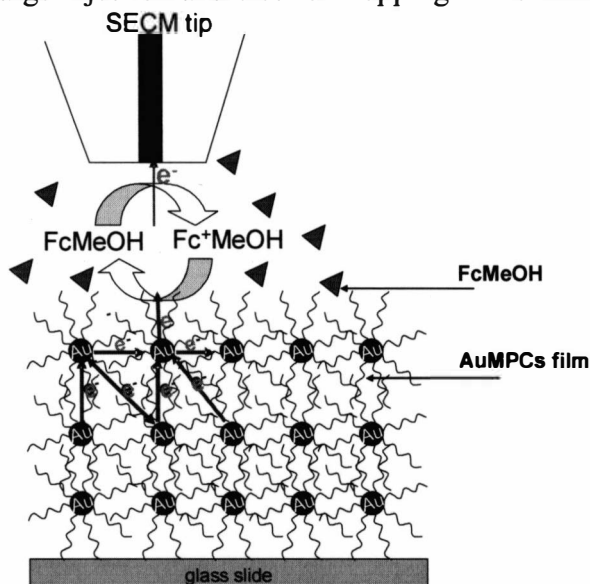


Figure 45 SECM investigations of electron transport in a drop-cast AuMPCs film on a glass substrate. The arrows depict possible electron transfer pathways through the film. The SECM tip is immersed in an electrolyte solution containing a redox mediator (FcMeOH).

Besides conductivity, other core-size-dependent properties have been observed for AuMPCs with 1-5 nm core diameter. For example Au_{38} (1.1 nm) exhibit a significant HOMO-LUMO gap (1.33 V) and becomes overtly molecule-like as evidenced by both

optical and electrochemical experiments⁶⁶. Larger Au₁₄₀MPC (1.6 nm) do not exhibit a significant HOMO-LUMO gap, but instead have such small capacitance (ca. 0.6 aF) that a series of evenly spaced one electron charging peaks can be observed^{19, 67}. This electronic core-charging phenomenon has been termed quantized double monolayer (QDL) charging. When Au cores are > 2 nm the discretized (one electron) double layer charging steps are smeared out.

5.1 Au₃₈(SC₆H₁₃)₂₄ – characterization and conductivity

The molecule-like hexalkanethiolate-protected Au₃₈ cluster described here was isolated based on its ethanol solubility from larger nanoparticles (see chapter II). A size-dependant opening of a HOMO-LUMO (the highest occupied and lowest unoccupied molecular orbitals) energy gap, representing the bulk-to-molecule transition, is specific for Au₃₈. Figure 46 displays a typical differential pulse voltammetry (DPV) of Au₃₈. DPV has been used extensively in AuMPCs studies, because the discrete electronic states peaks are better defined in differential pulse (or square wave) voltammetry than in CV. The pattern of electrochemical peaks consisting of three oxidation peaks (0/+1, +1/+2, and +2/+3) and one reduction peak (0/-1) with potential gaps as shown in Figure 46, is in good agreement with the literature values⁶⁶ for the same gold core.

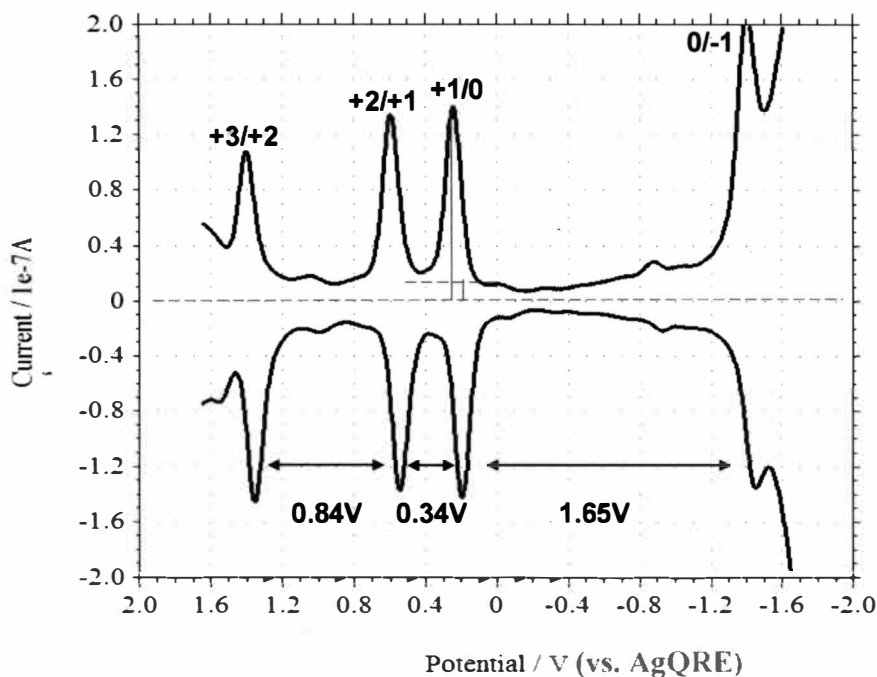
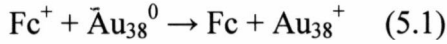


Figure 46 Differential pulse voltammetry (DPV) of 0.4 mM $\text{Au}_{38}(\text{SC}_6\text{H}_{13})_{24}$ in 0.1 M $\text{Bu}_4\text{NClO}_4/\text{CH}_2\text{Cl}_2$ at 0.4 mm Pt working electrode.

Various core-sized MPCs produces featureless background charging current underlying the DPV peaks⁶⁸. Hence monodispersity can be estimated by comparing the DPV peak current with the background current, which gave 92% monodispersity. Monodispersity is a key factor for observing conductivity in solid-state MPCs and the fine in size Au_{38} film revealed its conductive properties.

The approach curves (current versus tip-substrate distance) in Figure 47 are averages of two experiments. The current at the SECM tip far from the substrate is scaled by the limiting current given in equation 3.2 ($i_{\text{tip}} = 4naFDc^b$). The tip current as a function of the tip-film distance would increase in result of electron transport between the Au_{38}MPC film and the redox mediator (FcMeOH) in the solution based on the reaction:



FcMeOH has more positive potential (0.18 V vs. Ag/AgCl) than Au₃₈MPC, which makes the reaction 5.1 thermodynamically favorable.

Figure 47 displays the concentration dependence of the feedback current. The observed feedback current is combination of the diffusion flux in the solution and the flux due to the electron hopping in the film. Equation 5.2 explains why the deviation from the negative feedback increases with decreasing redox mediator concentration.

$$I = \frac{i_{tip}}{i_{tip,\infty}} \quad (5.2)$$

where I is the normalized tip current, i_{tip} is the feedback current along the approach, and $i_{tip,\infty}$ is the limiting current ($i_{tip,\infty} \propto c^b$ from equation 3.2).

The limiting current is proportional to the FcMeOH concentration, hence for a given feedback current, i_{tip} , lowering the redox mediator concentration, c^b , in the solution will increase the dimensionless current, I . This indicates that in order to observe the electron hopping process in the film (positive feedback), the redox mediator concentration needs to be reduced.

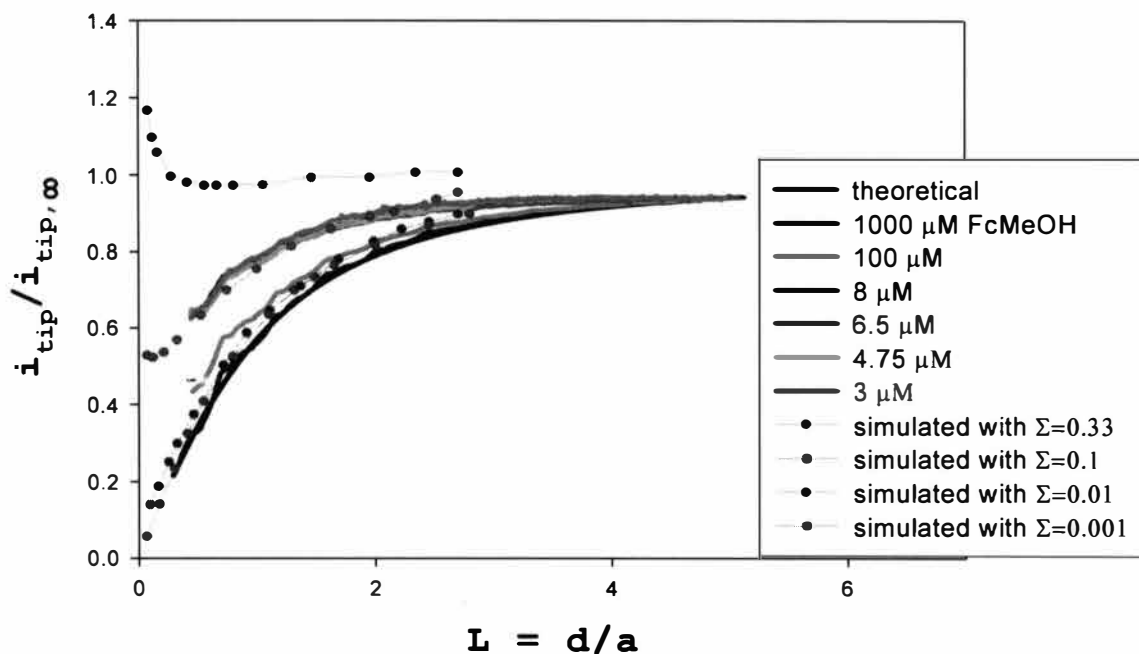


Figure 47 Experimental approach curves (solid lines) to Au_{38} films, where normalized tip current is plotted as a function of tip-film distance at different redox mediator concentrations (from bottom to top: 1000, 100, 8, 6.5, 4.75, and 3 μM), and simulated approach curves (circles) generated with different values of the dimensionless conductivity Σ (from bottom to top: 0.001, 0.01, 0.1, 0.33) taken from Quinn's work³.

In Figure 47 the approach curves taken at high redox mediator concentrations (1000 and 100 μM) show negative feedback due to hindered diffusion to the SECM tip (chapter III). Further reducing of the redox mediator concentration exposes a deviation from the pure negative feedback current. That deviation is apparent at 8, 6.5, 4.75, and 3 μM .

In fact, the deviation from 8 to 3 μM was not gradual as in the case of the larger 2.69 nm AuMPCs (this film A is discussed later), but rather a maximum contribution from the electron hopping was achieved at 8 μM and the following mediator decreasing

did not revealed any further conductivity increase. The observed feedback saturation, as the mediator concentration was lowered, has been predicted by the Quinn's model in a case of kinetic control⁶⁹. Hence, the kinetics of the electron transfer between the solution redox mediator and the small in size Au₃₈ nanoparticles (high charging energy) involved in reaction 5.1 could be a possible reason for the observed feedback response with redox mediator concentrations lower than 8 μM .

All four red curves (circles) in Figure 47 are digitized data from the theoretical model of the Quinn's group³. Their model assumes that the conduction current is directly proportional to the local electrochemical potential gradient. Despite the complexity of the model, in the end the fitting only involves one parameter, the film conductivity, Σ . A series of approach curves have been generated for various film conductivities³. These were used here to fit the experimental response as can be seen in Figure 47. The dimensionless conductivity Σ in the film is given by the equation³:

$$\Sigma = \frac{\sigma k T \Delta z}{e^2 a D c^b N_A} \quad (5.1)$$

where σ is conductivity, k is the Boltzmann constant, T is the absolute temperature, Δz is the film thickness, e is the elementary charge, a is the electrode radius, D is the redox mediator diffusion coefficient, c^b is the bulk concentration of the redox mediator, and N_A is the Avogadro constant.

Figure 48 shows the obtained dimensionless conductivities, Σ , from the fit in Figure 47 ($\Sigma=0.001$, 0.01, and 0.1) as a function of the inverse of the solution redox mediator concentration. From the slope of the linear fit was estimated the film conductivity $\sigma = 2.5 \times 10^{-8} \Omega^{-1} \text{cm}^{-1}$, which is comparable to a previous report ($6.1 \times 10^{-9} \Omega^{-1} \text{cm}^{-1}$) for a similar system⁷⁰. The Au₃₈ film here was prepared in the same manner as in

the reference [12] and the reported thickness of 1 μm was adopted for the σ calculation in equation 5.1.

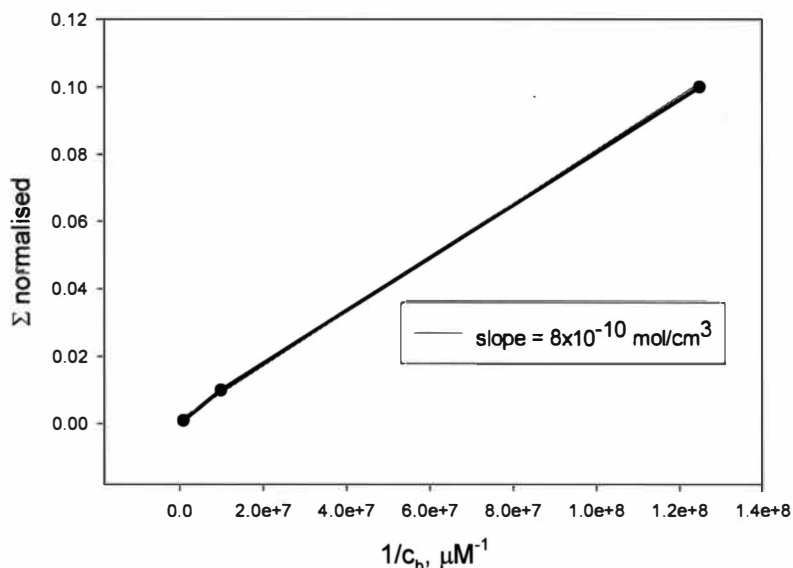


Figure 48 Dimensionless conductivity Σ as a function of the inverse of the solution redox mediator concentration.

Taking into account the uncertainties from the two different techniques – here a surface probe technique SECM was employed and Murray and coworkers⁷⁰ have been used an array electrode (IDA) – the obtained conductivities are in a good agreement.

5.2 $\text{Au}_{140}(\text{SC}_6\text{H}_{13})_{53}$ – characterization and conductivity

The interparticle distance ($d/2a$ in Figure 44) in Au_{140} sample was estimated to be less than the distance in Au_{38} sample, 1.6 and 1.8 respectively. The electron hopping conductivity was expected to be higher for Au_{140} , because of the enhanced core-core coupling. Figure 49 shows the results from the performed SECM experiments.

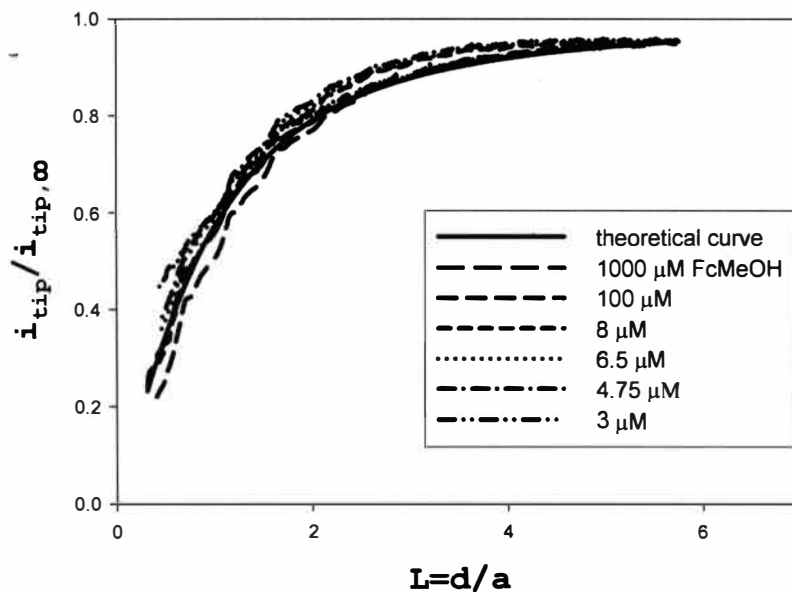


Figure 49 Experimental approach curves to Au₁₄₀ film, where normalized tip current is plotted as a function of tip-film distance at different redox mediator concentrations: 1000, 100, 8, 6.5, 4.75, and 3 μ M. The theoretical curve (solid line) was calculated from equation 3.6.

In contrast to our expectation, no deviation from pure negative feedback was observed with the concentration decreasing, opposite to the Au₃₈ film. There were small fluctuations, within the experimental error, of the experimental approach curves around the theoretical curve (solid line) for pure negative feedback (calculated with equation 3.6). The same SECM response was also recorded for a bare glass substrate in the same concentration range.

Au₁₄₀ has a core size of 1.6 nm and the coupling between the particles is not that strong as for the larger nanoparticles building a metal like nanocrystal lattice. Therefore even small disorder in its lattice leads to a cut off of the electron transport in a size polydisperse system.

To explain why some of the nanocrystal arrays exhibit only insulating behavior,

while some exhibit a metal-insulator transition, Remacle and Levine's performed quantum mechanical calculations for nanoparticles arrays, that explicitly account for the disorder that can result from the varied charging energies in a collection of size-polydisperse nanocrystals⁷¹. Disorder undoubtedly has played a central role in determining the nature of electron transport through nanocrystal lattices. The DPV in Figure 50 gives a monodispersity of 63 % for Au₁₄₀ sample, extracted by comparing the DPV peak current height of the first oxidation with the background current⁶⁷. Therefore this sample was considered rather polydisperse in comparison to Au₃₈ (92%).

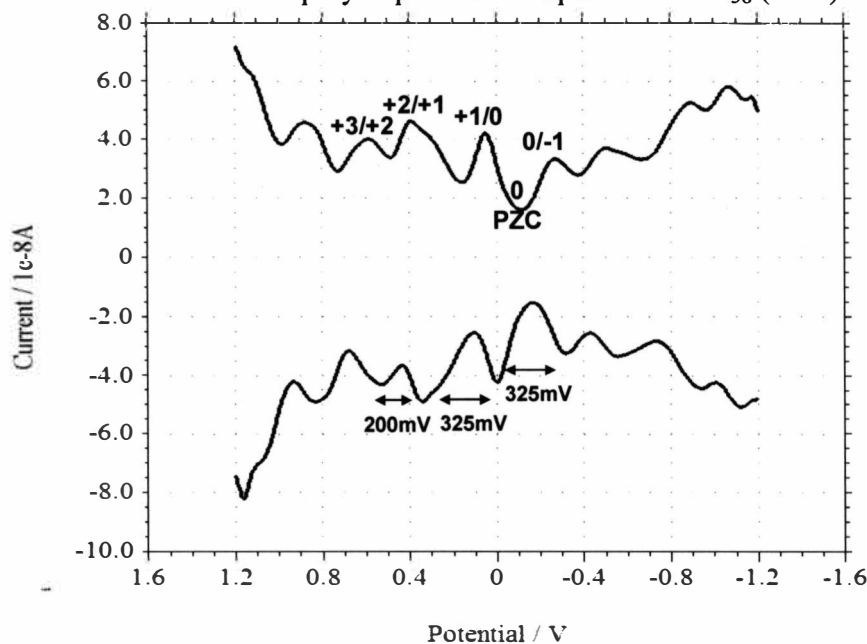


Figure 50 Differential pulse voltammetry (DPV) of 0.4 mM Au₁₄₀(SC₆H₁₃)₅₃ in 0.1 M Bu₄NClO₄/CH₂Cl₂ at 0.4 mm Pt working electrode and an Ag wire as a quasireference electrode. The potential of zero charge (PZC) is indicated in the figure.

Additionally, a sign of polydispersity can be seen in the pattern of the electrochemical peaks in Figure 50. The irregularity of the one electron current peaks,

otherwise near evenly spaced in a monodisperse sample (80 %) ⁶⁷, could originate from significant populations of very small nanoparticles. Their charging pattern would yield peaks with a large electrochemical gap or would overlap and enhance the peaks from Au₁₄₀. The first effect is unlikely to be seen on the voltammogram, because the extra peaks from the smaller particles cannot create gaps in an existing pattern, but a distortion of the DPV could occur due to the overlap. The presence of larger MPCs would lead to enhanced background current and the DPV peaks become blurred out, which is observed partially in Figure 50.

5.3 Conductivity of samples A and B

Furthermore, two larger core size samples were investigated for their conductivity by the SECM. Samples A and B are similar on an average size 2.69 ± 0.41 nm and 2.66 ± 0.68 nm, which gives equal interparticle separation ($d/2a=1.3$, Figure 44). However, the difference in their size distributions (see Figure 12) with coefficients of variance of 15.2 % and 25.6 % respectively, was found to have a pronounced effect on the electron transport in their films.

Figure 51 displays the concentration dependence of the approach curves taken to film A. As the concentration of the redox mediator was lowered from 1000 to 3 μM , positive feedback was obtained due to electron self-exchange inside the film.

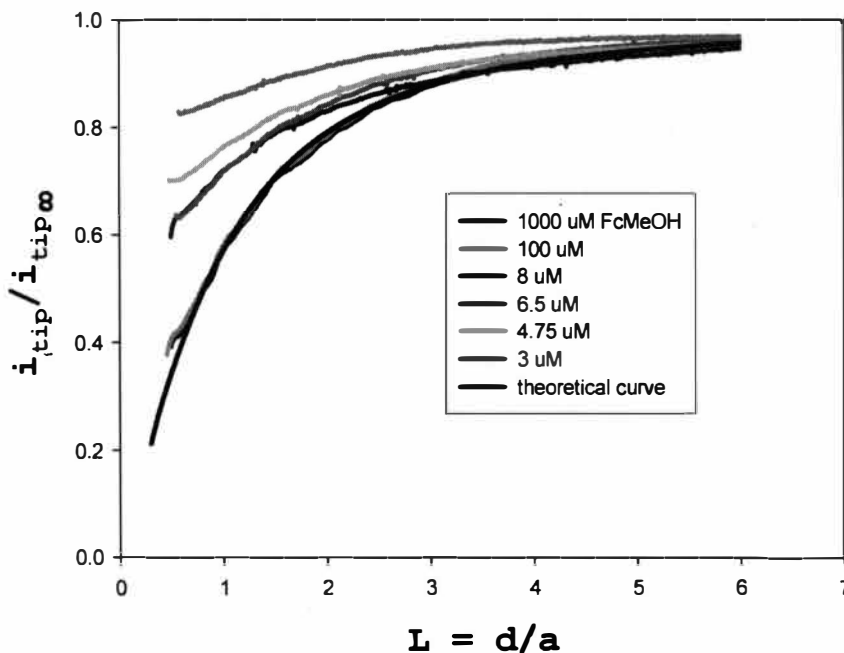


Figure 51 Experimental approach curves to film A, where normalized tip current is plotted as a function of tip-film distance at different redox mediator concentrations (from bottom to top: 1000, 100, 8, 6.5, 4.75, and 3 μM), and the theoretical curve calculated from equation 3.6.

Similar to the results attained to Au_{38} film, at the high concentrations 1000 and 100 μM , generated approach curves show negative feedback. However, further reducing of the mediator concentration (from 8 to 3 μM) leads to a gradual increase of the feedback current reflecting amplified contribution of A film conductivity. Pure positive feedback was not observed in the case of larger A probably due to exceedingly low concentration and currents needed to reach this regime, but the deviation from the negative feedback at 3 μM was greater for sample A in comparison to Au_{38} sample. This size effect resulting in an electron transport rate dependency, could be explained by the charging energy⁷².

Figure 52 illustrates the origin of the size-effect observed with samples A and

Au₃₈. This size-effect can be described by combining equations 1.3 and 1.4, solved for the charging energy, E_c :

$$E_c = \frac{e^2}{4\pi\epsilon_0\epsilon} \left(\frac{d}{r} \right) \left(\frac{1}{r+d} \right) \quad (5.2)$$

where e is the electronic charge, ϵ_0 is the permittivity of free space, ϵ is the dielectric constant of the monolayer, r is the core radius, and d is the distance between two particles.

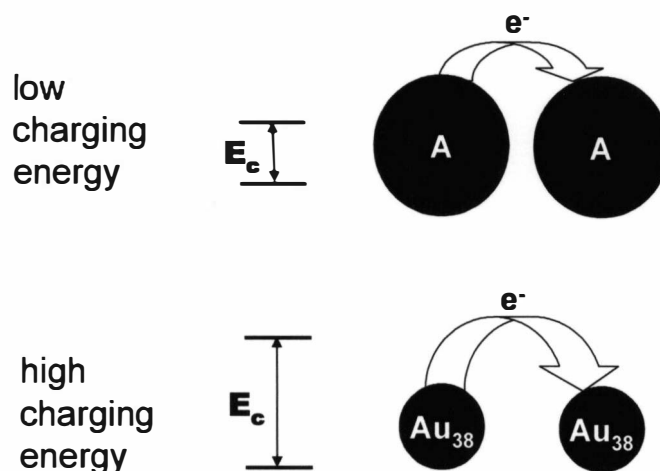


Figure 52 Schematic of the electron transport between particles with different core size.

For the larger nanoparticles (sample A, short interparticle separation), electrons are delocalized over several particles as in a metal. The charging energy, which is the energy required to remove an electron from one isolated particle to another isolated particle, is insignificant. Contrary, the charging energy is higher for the smaller particles (Au₃₈, long interparticle separation in addition) and the charging energy cost to inject an electron to an individual particle must be overcome. The presence of this extra barrier decreases the rate of electron transfer.

The UV-VIS spectra of sample A and sample B (Figure 11) show that B contains

a great population of larger particles (the highest surface plasmon band intensity) compared to A. Hence, the electronic coupling (related to conductivity) in film B should be stronger than in film A.

Figure 53 shows the current versus tip-film distance curves obtained during the SECM experiment to film B, where only negative feedback was observed. The approach curves were recorded to film B in the same concentration range (from 1000 to 3 μM). The most reasonable explanation of not having similar response for the conductivity from both films (A and B) lies in their different size distributions (coefficients of variance 25.6 % versus 15.2 %). In result, the occurrence of small and big particles caused a local disorder.

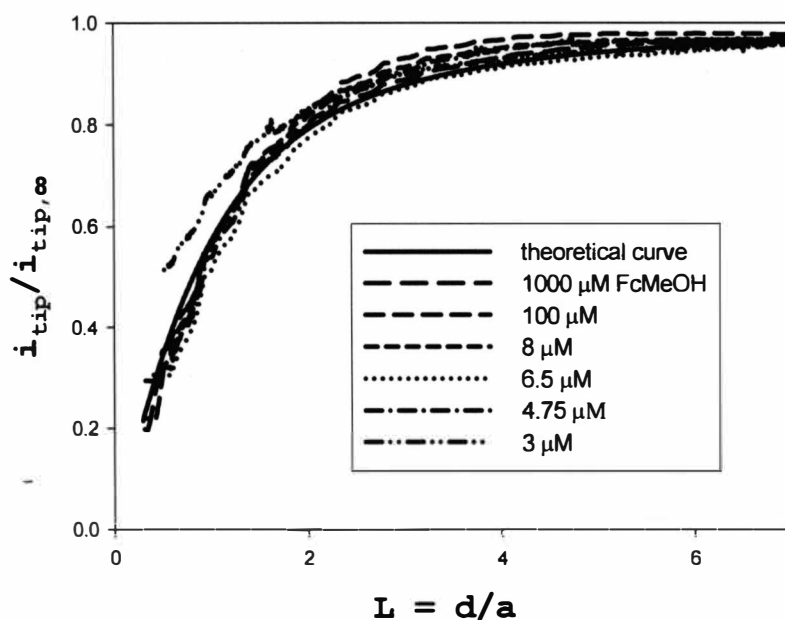


Figure 53 Examples of experimental approach curves to film B, where normalized tip current is plotted as a function of tip-film distance at different redox mediator concentrations: 1000, 100, 8, 6.5, 4.75, and 3 μM and a theoretical curve calculated from equation 3.6.

The presence of the polydispersity in sample B prevents obtaining of a spatially organized gold nanoparticle lattice and as expected in the system with some disorder, a rise to an Anderson-type localized insulator was given⁷¹. The electron coupling between the particles is weak, the electrons remain localized, and the lattice behaved as an insulator.

The local disorder may play a significant role in the electron hopping process as seen in the case of sample B. Figure 54 depicts the electron pathways in a well ordered lattice (a) and in a polydisperse lattice (b).

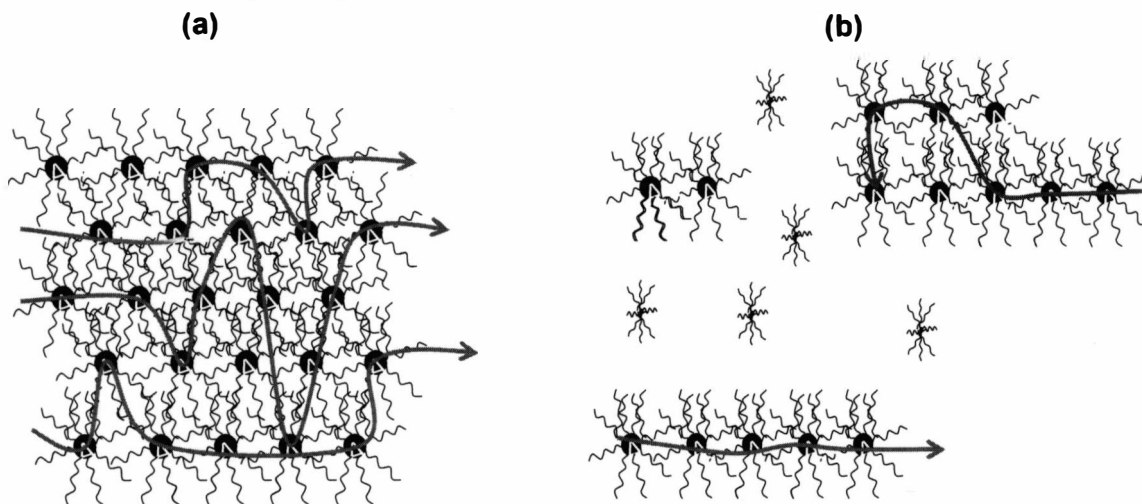


Figure 54 Electron transport through a gold nanoparticle film: (a) ordered lattice and (b) disordered lattice.

When the particles are in close proximity, the electron coupling is strong and the electron pathways are unrestricted over the film, exhibiting metallic properties. On the other hand, the local disorder causes discontinued electron pathways, displaying insulating behavior.

CHAPTER VI

CONCLUSIONS AND FUTURE DIRECTIONS

Isotherm Investigation

Saturated lipids were more stable than the unsaturated ones.

The size of the dye molecule (NBD-PE) was very close to that of the DMPC lipid molecule and thus caused no distortion of the lipid matrix.

Deposition

Deposition of lipid onto a hydrophilic substrate was found to be easier than onto hydrophobic one. The deposition was conducted at high and low surface pressure (25-45 mN/m) on a hydrophilic substrate, while only at high surface pressure (45 mN/m) on a hydrophobic substrate.

Fluorescence

Fluorescence spectroscopy and microscopy of the dye-lipid system showed successful deposition and uniform distribution of the monolayer on a micrometer scale.

Contact Angle

The monolayer of mixed DmFc-lipid was found to be stable. Monolayer quality, however, is not suitable for studying the electron transport.

Electrochemistry with a modified ITO

The presence of DmFc in the lipid monolayer was proved by the experiment with a modified ITO macroelectrode.

The monolayer used for modifying an ITO was not sufficient to block electroactive species outside the monolayer. This result also suggested the presence of defects in the monolayer.

Continuous monitoring of the monolayer transfer could provide more uniform

monolayers. Structural parameters for transferred monolayer on a solid substrate could be obtained using a Brewster angle microscopy as a complementary technique for Langmuir-Bodgett studies.

SECM and mixed DmFc-lipid substrate

The system of the lipid monolayer with freely diffusing decamethylferrocene inside (DmFc-lipid system) was not trivial, rather challenging. It can be regarded as one of two intensive fields of study – electron transport at the liquid/liquid interface (related to physical diffusion of the electroactive species) and long-range electron transport through hydrocarbon chains as in the alkanethiolate self-assembled monolayers (related to an electron tunneling mechanism). There are numerous factors that influence the electron transport through the DmFc-lipid monolayer, studied by the SECM, such as electron transfer between DmFc molecules in the lipid, bimolecular electron transport between DmFc and the redox mediator in the aqueous phase, electron transfer between the redox mediator molecules, and ion permeation in the monolayer. All of these factors were considered and optimized, but further work is needed.

Simulation

The simulation of the electron transport in a gold nanoparticle film coupled with charge transport to the SECM tip resulted in solving the diffusion problem at a disk microelectrode and solving the electron transfer reaction problem between the solution redox couple and the nanoparticle film. Solving the electron transport in the film was left for future investigations.

SECM and Au₃₈ film

The electronic conductivity of Au₃₈ film was found to be $2.5 \times 10^{-8} \Omega^{-1} \text{cm}^{-1}$. Kinetic limitation could be a factor for the observed conductivity saturation with

decreasing redox mediator concentration.

SECM and Au₁₄₀ film

Au₁₄₀ film behaved as an insulator due to its polydispersity. A low monodispersity of 63 % was found from its differential pulse voltammogram.

The electronic conductivity in film A, a qualitative estimation, was the highest from all the samples investigated. A gradual increase of the feedback current was recorded with decreasing the redox mediator concentration.

SECM and films A and B

Film B behaved as an insulator in contrast to film A, regardless their same averaged core sizes. The disorder effect in sample B was found to be the main reason for this behavior.

Further decreasing of the redox mediator concentration in the SECM experiment with film A would decrease the electron transport between the redox mediator molecules and would reveal the lateral electron transport contribution. Positive feedback with this film would be possible to obtain with an instrument with lower than 1 pA current measurability.

The conductivity appears to be dependent on the MPC core size as seen from film A and Au₃₈, but the dependence becomes weaker with core size dispersity.

In order to understand better the electron transport mechanism in nanoparticle films, new approaches for monodisperse AuMPCs isolation are needed. Studying the variety of narrow core size AuMPCs samples will give more insight into their size-dependent conductive properties.

By using different redox mediators, it will be possible to observe reaction rate dependencies between the redox mediator and the nanoparticles.

Monolayer protected clusters, MPCs, functionalized with redox groups are also interesting as they provide a platform to examine MPC materials in the context of multielectron transfer.

Development of another mode of SECM operation such as surface mapping would give additional information about the surface events of the investigated samples.

REFERENCES

1. CH-Instruments, <http://www.chinstruments.com/chi900.html>.
2. Ruiz, V.; Liljeroth, P.; Quinn, B. M.; Kontturi, K., Probing conductivity of polyelectrolyte/nanoparticle composite films by scanning electrochemical microscopy. *Nano Letters* 2003, 3, (10), 1459-1462.
3. Liljeroth, P.; Vanmaekelbergh, D.; Ruiz, V.; Kontturi, K.; Jiang, H.; Kauppinen, E.; Quinn, B. M., Electron Transport in Two-Dimensional Arrays of Gold Nanocrystals Investigated by Scanning Electrochemical Microscopy. *Journal of American Chemical Society* 2004, 126, 7126-7132.
4. Liu, H.-Y.; Fan, F.-R. F.; Lin, C. W.; Bard, A. J., Scanning Electrochemical and Tunneling Ultramicroelectrode Microscope for High-Resolution Examination of Electrode Surfaces in Solution. *J. Am. Chem. Soc.* 1986, 108, 3838-3839.
5. Bard, A. J.; Mirkin, M. V., Scanning Electrochemical Microscopy. *New York: Marcel Dekker* 2001.
6. Wightman, R. M., Microvoltammetric electrodes. *Anal. Chem.* 1981, 53, 1125 A-1134 A.
7. Kwak, J.; Bard, A. J., Scanning electrochemical microscopy. Theory of the feedback mode. *Analytical Chemistry* 1989, 61, (11), 1221-7.
8. Tsionsky, M.; Bard, A. J.; Mirkin, M. V., Long-Range Electron Transfer through a Lipid Monolayer at the Liquid/Liquid Interface. *J. Am. Chem. Soc.* 1997, 119, 10785-10792.
9. Tsionsky, M.; Zhou, J.; Amemiya, S.; Fan, F.-R. F.; Bard, A., Scanning electrochemical microscopy: 38. Application of SECM to the study of charge transfer through bilayer lipid membranes. *Anal. Chem.* 1999, 71, 4300-4305.
10. Forster, R. J., Microelectrodes—Retrospect and Prospect Encyclopedia of Electrochemistry. *Instrumentation and Electroanalytical Chemistry vol 3, New York: Wiley* 2003, 160-195.
11. Zoski, C. G., Ultramicroelectrodes: design, fabrication, and characterization. *Electroanalysis* 2002, 14, 1041-1051.
12. Macpherson, J. V.; Unwin, P. R., Noncontact electrochemical imaging with combined scanning electrochemical-atomic force microscopy. *Anal. Chem.* 2001, 73, 550-557.
13. Macpherson, J. V.; Unwin, P. R., Combined scanning electrochemical-atomic force microscopy. *Anal. Chem.* 2000, 72, 276-285.
14. Davis, W. B.; Svec, W. A.; Ratner, M. A.; Wasielewski, M. R., Molecular-wire behaviour in p -phenylenevinylene oligomers. *Nature* 1998, 396, 60-63.
15. Fox, M. A., Fundamentals in the Design of Molecular Electronic Devices: Long-Range Charge Carrier Transport and Electronic Coupling. *Acc. Chem. Res.* 1999, 32, 201 - 207.

16. Low, P. J., Metal complexes in molecular electronics: progress and possibilities. *Dalton Transaction* 2005, 2821.
17. Barbara, P. F.; Meyer, T. J.; Ratner, M. A., Contemporary Issues in Electron Transfer Research. *J. Phys. Chem.* 1996, 100, 13148 - 13168.
18. Kastner, M. A., The single-electron transistor. *Rev. Mod. Phys.* 1992, 64, 849-858.
19. Hicks, J. F.; Templeton, A. C.; Chen, S.; Sheran, K. M.; Jasti, R.; Murray, R. W.; Debord, J.; Schaaff, T. G.; Whetten, R. L., The Monolayer Thickness Dependence of Quantized Double-Layer Capacitances of Monolayer-Protected Gold Clusters. *Anal. Chem.* 1999, 71, 3703.
20. Ginger; Greenham, Electrical properties of semiconductor nanocrystals. *Semiconductor and metal nanocrystals: Marcel Dekker* 2004, 265-288.
21. Zabet-Khosousi, A.; Trudeau, P.-E.; Suganuma, Y.; Dhirani, A.-A., Metal to Insulator Transition in Films of Molecularly Linked Gold Nanoparticles. *Phys. Rev. Lett.* 2006, 96, 156403.
22. Anderson, P. W., Absence of diffusion in certain random lattices. *Phys. Rev. Lett.* 1958, 109, 1492-1505.
23. Trudeau, P.-E.; Escorcia, A.; Dhirania, A.-A., Variable single electron charging energies and percolation effects in molecularly linked nanoparticle films. *J. Chem. Phys.* 2003, 119, 5267-5273.
24. KRUSS, DSA1 v 1.80/ Drop Shape Analysis. *User Manual V030621* 2002, 183.
25. Whightman, R. M. a. W., D. O., Electrochemical Chemistry. 1988, 15, 267.
26. Mirkin, M. V., Fan, F. F., and Bard, A. J., *J. Electroanal. Chem.* 1992, 328, 47.
27. Lee, C., Miller C. J., and Bard, A. J., *Analytical Chemistry* 1991, 63, 78.
28. Fleischmann, M., Pons, S., Rolinson, D. R., and Schmidt, P. P., *Ultramicroelectrodes*. ed.; Datatech Systems: Morgantown, NC, 1987; 'Vol.' p.
29. Brust, M., Wlker, Marryl, Bethel Donald, Schiffrin David, Whyman, Robin, Synthesis of thiol-derivatised gold nanoparticales in a two-phase liquid-liquid system. *J. Chem. Soc., Chem. Commun.* 1994, 801.
30. Hostetler, M., Wingate, J., Zhong, C., Harris, J., Vachet, R., Clark, M., Londono, J., Green, S., Stokes, J., Wignall, G., Glish, G., Porter, M., Evans, N., and Murray, R., Alkanethiolate gold cluster molecules with core diameters from 1.5 to 5.2 nm: core and monolayer properties as a function of core size. *Langmuir* 1998, 14, 17.
31. Lee, D.; Donkers, R. L.; DeSimone, J. M.; Murray, R. W., Voltammetry and Electron-Transfer Dynamics in a Molecular Melt of a 1.2 nm Metal Quantum Dot. *J. Am. Chem. Soc.* 2003, 125, 1182-1183.
32. Bard, A. J.; Fan, F.-R. F.; Kwak, J.; Lev, O., Scanning Electrochemical Microscopy. Introduction and Principles. *Analytical Chemistry* 1989, 61, 132-138.
33. Wipf, D. O.; Bard, A. J., Scanning electrochemical microscopy. X. Resolution imaging of active sites on an electrode surface. *Journal of the Electrochemical Society* 1991, 138, (5), L4-L6.
34. Bard, A. J.; Mirkin, M. V.; Unwin, P. R.; Wipf, D. O., Scanning electrochemical microscopy. 12. Theory and experiment of the feedback mode with finite

- heterogeneous electron-transfer kinetics and arbitrary substrate size. *Journal of Physical Chemistry* 1992, 96, (4), 1861-8.
35. Kwak, J.; Bard, A. J., Scanning electrochemical microscopy. Apparatus and two-dimensional scans of conductive and insulating substrates. *Analytical Chemistry* 1989, 61, (17), 1794-9.
 36. Bond, A. M.; Oldham, K. B.; Zoski, C. G., Steady-state voltammetry. *Analytica Chimica Acta* 1989, 216, (1-2), 177-230.
 37. Mirkin, M. V.; Bard, A. J., Multidimensional integral equations: a new approach to solving microelectrode diffusion problems. Part 2. Applications to microband electrodes and the scanning electrochemical microscope. *Journal of Electroanalytical Chemistry* 1992, 323, (1-2), 29-51.
 38. Unwin, P. R.; Bard, A. J., Scanning electrochemical microscopy. 14. Scanning electrochemical microscope induced desorption: a new technique for the measurement of adsorption/desorption kinetics and surface diffusion rates at the solid/liquid interface. *Journal of Physical Chemistry* 1992, 96, (12), 5035-45.
 39. Mirkin, M. V.; Fan, F. R. F.; Bard, A. J., Scanning electrochemical microscopy. Part 13. Evaluation of the tip shapes of nanometer size microelectrodes. *Journal of Electroanalytical Chemistry* 1992, 328, (1-2), 47-62.
 40. Amphlett, J. L.; Denuault, G., Scanning Electrochemical Microscopy (SECM): An Investigation of the Effects of Tip Geometry on Amperometric Tip Response. *Journal of Physical Chemistry B* 1998, 102, (49), 9946-9951.
 41. Amemiya, S., Solving 2D Diffusion problem at Disk UME by FEMLAB. 2005, FEMLAB class handout University Pittsburgh.
 42. COMSOL_Multiphysics_Model_Library, Chemical Engineering Models; Model Library Path: COMSOL_Multiphysics/Chemical_Engineering/adsorption. Chapter 3: p30.
 43. Bard, A.; Faulkner, L., Electrochemical methods. *John Wiley & Sons, Inc* 2001.
 44. Zhang, J.; Unwin, P. R., Kinetics of IrCl₆²⁻ ion transfer across the water/1,2-dichloroethane interface and the effect of a phospholipid monolayer. *Langmuir* 2002, 18, 2313-2318.
 45. Zhang, J.; Unwin, P. R., Kinetics of bromine transfer across Langmuir monolayers of phosphatidylethanolamines at the water/air interface. *Phys. Chem. Chem. Phys.* 2003, 5, 3979-3983.
 46. Strutwolf, J.; Zhang, J.; Barker, A. L.; Unwin, P. R., Effect of phospholipids on the kinetics of dioxygen transfer across a 1,2-dichloroethane/water interface. *Chem. Chem. Phys.* 2001, 3, 5553-5558.
 47. Cannan, S.; Zhang, J.; Grunfeld, F.; Unwin, P. R., Scanning electrochemical microscopy (SECM) studies of oxygen transfer across phospholipid monolayers under surface pressure control: comparison of monolayers at air/water and oil/water interfaces. *Langmuir* 2004, 20, 701-707.
 48. Martin, P.; Szablewski, M., Langmuir-Blodgett troughs. *Nima technology Ltd*. 2002.

49. Avanti Polar Lipids, I.
<http://www.avantilipids.com/PhaseTransitionTemperaturesGlycerophospholipids.html>.
50. Moehwald, H., Handbook of Biological Physics. 1995, Elsevier Science B. V.
51. Lee, Y.-L.; Chen, C.-Y., Surface wettability and platelet adhesion studies on Langmuir-Blodgett films. *Applied Surface Science* 2003, 207, 51.
52. Birdi, K. S., Self-Assembly Monolayer Structures of Lipids and Macromolecules at Interfaces. *Kluwer Academic/Plenum Publishers* 1999.
53. Haugland, R., Handbook of Fluorescent Probes and Research Products. *Molecular Probes* 2002.
54. Edidin, M., Molecular motions and membrane organization and function. *Membrane structure* 1981, Chapter 2, 37.
55. Richardson, J. N.; Harvey, J.; Murray, R. W., Heterogeneous Electron-Transfer Dynamics of Decamethylferrocene from 130 to 181 K. 1994, 98, 13396-13402.
56. Isichenko, M. B., Percolation, statistical topography, and transport in random media. *Rev. Mod. Phys.* 1992, 64, 961-1042.
57. Liljeroth, P.; Quinn, B. M.; Ruiz, V.; Kontturi, K., Charge injection and lateral conductivity in monolayers of metallic nanoparticles. *Chemical Communications (Cambridge, United Kingdom)* 2003, (13), 1570-1571.
58. Lin, J. C.; Chuang, J., *J. Biomed. Mater. Res.* 2000, 51, 413.
59. Anariba, F.; Steach Jeremy, K.; McCreery Richard, L., Strong effects of molecular structure on electron transport in carbon/molecule/copper electronic junctions. *The journal of physical chemistry. B, Condensed matter, materials, surfaces, interfaces & biophysical* 2005, 109, (22), 11163.
60. Reinhardt-Schlegel, H.; Kawamura, Y.; Furuno, T.; Sasabe, H., *J. Colloid Interface Sci.* 1991, 147, 295.
61. Seitz, M., *Thin solid films* 1998, 327, (329), 767.
62. Quinn, B. M.; Prieto, I.; Haram, S. K.; Bard, A. J., Electrochemical Observation of a Metal/Insulator Transition by Scanning Electrochemical Microscopy. *J. Phys. Chem. B* 2001, 105, 7474 - 7476.
63. Ruiz, V.; Liljeroth, P.; Quinn, B. M.; Kontturi, K., Probing Conductivity of Polyelectrolyte/Nanoparticle Composite Films by Scanning Electrochemical Microscopy. *Nano Letters* 2003, 3, 1459-1462.
64. Markovich, G.; Collier, C. P.; Heath, J. R., Reversible metal-insulator transition in ordered metal nanocrystal monolayers observed by impedance spectroscopy. *Phys. Rev. Lett.* 1998, 80, 3807-3810.
65. Wuelfing, W. P.; Green, S. J.; Pietron, J. J.; Cliffel, D. E.; Murray, R. W., Electronic conductivity of solid-state, mixed-valent, monolayer-protected Au clusters. *J. Am. Chem. Soc.* 2000, 122, 11465-11472.
66. Lee, D.; Donkers, R. L.; Harper, A. S.; Wang, G.; Murray, R. W., Electrochemistry and Optical Absorbance and Luminescence of Molecule-like Au₃₈ Nanoparticles. *J. Am. Chem. Soc.* 2004, 126, 6193-6199.

67. Hicks, J. F.; Miles, D. T.; Murray, R. W., Quantized Double-Layer Charging of Highly Monodisperse Metal Nanoparticles. *J. Am. Chem. Soc.* 2002, 124, 13322-13328.
68. Hicks, J. F.; Zamborini, F. P.; Osisek, A. J.; Murray, R. W., The Dynamics of Electron Self-Exchange between Nanoparticles. *J. Am. Chem. Soc.* 2001, 123, 7048.
69. Liljeroth, P.; Quinn, B. M., Resolving Electron Transfer Kinetics at the Nanocrystal/Solution Interface. *J. Am. Chem. Soc.* 2006, 128, 4922-4923.
70. Choi, J.-P.; Murray, R. W., Electron self-exchange between Au₁₄₀⁺⁰ nanoparticles is faster than that between Au₃₈⁺⁰ in solid-state, mixed-valent films. 2006, 128, 10496-10502.
71. Remacle, F.; Levine, R. D., Electronic Response of Assemblies of Designer Atoms: The Metal-Insulator Transition and the Role of Disorder. *J. Am. Chem. Soc.* 2000, 122, 4084-4091.
72. Markovich, G.; Collier, C. P.; Henrichs, S. E.; Remacle, F.; Levine, R. D.; Heath, J. R., Architectonic Quantum Dot Solids. *Acc. Chem. Res.* 1999, 32, 415-433.

APPENDIX A

MATLAB PPROGRAM

Comsol Multiphysics was connected to MatLab for simulation of the approach by the SECM tip. MatLab was used for varying the distance between the tip and the substrate from 30 to 0.1 μm . Comsol was used for solving of the diffusion problem to the tip. The whole program, extracted by applying the software (Comsol and Matlab), is shown below.

```
flclear fem
clear;
clc;
close all;

nv=25; % How many points
dv_ulim=30e-6/12.5e-6; % Upper limit for dv
dv_llim=0.1e-6/12.5e-6; % Lower limit for dv
dv_range=dv_ulim-dv_llim; % Range of change of dv
dv_step=dv_range/nv; % How much to changedv every step

for iv=1:nv
    iv
```

```

dv(iv)=dv_llim+dv_step*iv;

mess=['Suobstenie ot gospodarja - " iteration number : ', ...

    num2str(iv),' "'];

```

```

% COMSOL version

```

```

clear vrsn

vrsn.name = 'COMSOL 3.2';

vrsn.ext = "";

vrsn.major = 0;

vrsn.build = 222;

vrsn.rcs = '$Name: $';

vrsn.date = '$Date: 2005/09/01 18:02:30 $';

fem.version = vrsn;

```

```

% Geometry

```

```

carr={curve2([0,1.0000],[0,0],[1,1]), ...

    curve2([1.0000,5.4000],[0,0],[1,1]), ...

    curve2([5.4000,5.4000],[0,20.0000],[1,1]), ...

    curve2([5.4000,25.4000],[20.0000,20.0000],[1,1]), ...

    curve2([25.4000,25.4000],[20.0000,-dv(iv)],[1,1]), ...

    curve2([25.4000,1.0000],[-dv(iv),-dv(iv)],[1,1]), ...

```

```

curve2([1,0],[-dv(iv),-dv(iv)],[1,1]), ...
curve2([0,0],[-dv(iv),0],[1,1]));
g1=geomcoerce('solid',carr);
g2=fillet(g1,'radii',4.0E-5/12.5e-6,'point',[5]);

```

% Constants

```

fem.const = {'cb','1', ...
'Dsol','0.25', ...
'Kf','0', ...
'Kb','0', ...
'y','40.61866667', ...
'Ds','0.434782609'};

```

% Geometry

```

clear s
s.objs={g2};
s.name={'CO2'};
s.tags={'g2'};

```

```

fem.draw=struct('s',s);
fem.geom=geomcsg(fem);

```



```

% Initialize mesh

minel=0.001e-4/12.5e-6;

fem.mesh=meshinit(fem, ...

    'haut0',7, ...

    'hgrad',1.2, ...

    'hmaxvtx',[3,minel,4,minel], ...

    'hmaxedg',[1,minel,2,minel,3,minel]);


% Application mode 1

clear appl

appl.mode.class = 'Diffusion';

appl.mode.type = 'axi';

appl.module = 'CHEM';

appl.assignsuffix = '_chdi';

clear bnd

bnd.type = {'N0','N','C','C','N'};

bnd.c0 = {0,0,0,'cb',0};

bnd.N = {0,0,0,0,'react_surf'};

bnd.ind = [1,5,3,2,1,1,4,4,1];

appl.bnd = bnd;

```

```

clear equ

equ.D = 'Dsol';

equ.init = 'cb';

equ.ind = [1];

appl.equ = equ;

fem.appl{1} = appl;


% Application mode 2

clear appl

appl.mode.class = 'FIPDEWBoundary';

appl.dim = {'cs','cs_t'};

appl.sdim = {'r','z','phi'};

appl.assignsuffix = '_wb';

clear prop

clear weakconstr

weakconstr.value = 'off';

weakconstr.dim = {'lm2','lm3'};

prop.weakconstr = weakconstr;

appl.prop = prop;

clear bnd

bnd.weak = {0,'Ds*(-csTx_test*csTx-csTy_test*csTy)+cs_test*react_surf'};

```

```
bnd.dweak = {0,'cs_test*cs_time'};
```

```
bnd.usage = {0,1};
```

```
bnd.ind = [1,2,1,1,1,1,1,1,1];
```

```
appl.bnd = bnd;
```

```
fem.appl{2} = appl;
```

```
fem.sdim = {'r','z'};
```

```
fem.border = 1;
```

```
fem.outform = 'general';
```

```
fem.units = 'SI';
```

```
% Boundary expressions
```

```
clear bnd
```

```
bnd.ind = [1,2,1,1,1,1,1,1,1];
```

```
bnd.dim = {'c','cs'};
```

```
bnd.expr = {'react_surf',{'Kf*c*(y-cs)-Kb*cs'}};
```

```
fem.bnd = bnd;
```

```
% Coupling variable elements
```

```
clear elemcpl
```

```
% Integration coupling variables
```

```
clear elem
```

```

elem.elem = 'elcplscalar';

elem.g = {'1'};

src = cell(1,1);

clear bnd

bnd.expr = {{{}, 'pi*2*r*ndflux_c_chdi'}};

bnd.ipoints = {{{}, '4'}};

bnd.ind = {'1','2','4','5','6','7','8','9'}, {'3'};

src{1} = {{}, bnd, {}};

elem.src = src;

geomdim = cell(1,1);

geomdim{1} = {};

elem.geomdim = geomdim;

elem.var = {'T'};

elem.global = {'1'};

elemcpl{1} = elem;

fem.elemcpl = elemcpl;

```

% Descriptions

```

clear descr

descr.const= {'Ds','surface diffusivity','Gama_max','total concentration of the active
sites','Dsol','FcMeOH diffusion coefficient','cb','bulk FcMeOH concentration'};

```

```

fem.descr = descr;

% Multiphysics
fem=multiphysics(fem);

% Extend mesh
fem.xmesh=meshtextend(fem);

% Show the geometry and the mesh
cla;

set(gcf,'color','w');

meshplot(fem, ...

    'boundmode', 'off', ...

    'elmode', 'on');

set(gca,'box','on');

axis equal;

xlabel('x [m]');

ylabel('y [m]');

mdim=max([get(gca,'ylim'),get(gca,'xlim')]);

axis([-mdim/4 5/4*mdim -mdim/4 5/4*mdim]);

drawnow;

```

```

% Solve problem

fem.sol=femtime(fem, ...

    'solcomp',{'c','cs'}, ...

    'outcomp',{'c','cs'}, ...

    'tlist',[0:100:100], ...

    'tout','tlist');


% Integrate the current on the electrode tip

Tok(iv)=postint(fem,'pi*2*r*(ndflux_c_chdi)', ...

    'dl',[3], ...

    'edim',1, ...

    'solnum','end');


%   waitbar(iv/nv,h);

end


% Plot the results

% close(h);

% close all;

plot(dv,Tok,'-k. ');

set(gcf,'color','w');

```

```
set(gca,'box','on');  
xlabel('dv [m]');  
ylabel('Tok [A]');  
grid on;
```

APPENDIX B

PERMISSION LETTER

From Bernadette Quinn <bquinn@iki.fi>
Sent Thursday, January 18, 2007 6:13 am
To Violeta A Stoycheva <violeta.stoycheva@wmich.edu>
Subject Re: permission

Dear Violeta

you have my permission to include the figures in your thesis.

Regards

Bernadette Quinn

Quoting Violeta A Stoycheva <violeta.stoycheva@wmich.edu>:

> Dear Dr. Quinn,

>

> I am a master student at Western Michigan University and I am

> writing to ask for your permission for using your work in my thesis.

> I found your results are very useful regarding the simulation in

> JACS, 2004, 126, p7126, figure S5*. Also I liked your schematic in

> Nano Letters, 2003, 3, p1459, figure S3*. I would like to include

> them in my thesis, if you would allow me.

>

> Thank you for your time.

>

> Sincerely,

> Violeta Stoycheva

>

>

> --

> Violeta Stoycheva

> Western Michigan University

> Chemistry Department

> tel. 269 387 2886

> e-mail: violeta.stoycheva@wmich.edu

*Note: For more details on the used references, refer to the references 3 and 63 under section 'REFERENCES' on page 84 in this thesis